NASA TECHNICAL NOTE

NASA TN D-3201



NASA TN D-3201

# AERODYNAMIC CHARACTERISTICS OF THE SHARP RIGHT CIRCULAR CONE AT MACH 20.3 AND ANGLES OF ATTACK TO 110° IN HELIUM

*by Dal V. Maddalon*

*Langley Research Center*
*Langley Station, Hampton, Va.*



NATIONAL AERONAUTICS AND SPACE ADMINISTRATION • WASHINGTON, D. C. • FEBRUARY 1966

# AERODYNAMIC CHARACTERISTICS OF THE SHARP RIGHT CIRCULAR CONE AT MACH 20.3 AND ANGLES OF ATTACK TO 110° IN HELIUM

By Dal V. Maddalon

Langley Research Center
Langley Station, Hampton, Va.

NATIONAL AERONAUTICS AND SPACE ADMINISTRATION

For sale by the Clearinghouse for Federal Scientific and Technical Information
Springfield, Virginia 22151 – Price $3.00

# AERODYNAMIC CHARACTERISTICS OF THE SHARP RIGHT CIRCULAR CONE AT MACH 20.3 AND ANGLES OF ATTACK TO 110° IN HELIUM

By Dal V. Maddalon
Langley Research Center

## SUMMARY

A study of the static longitudinal aerodynamic characteristics of the sharp right circular cone at a Mach number of 20.3 and a Reynolds number of $0.37 \times 10^6$ per inch $(14.6 \times 10^6$ per meter) in helium has been conducted. Results of the investigation were compared with exact theory, Cheng's cone theory, Newtonian theory, and existing data obtained in air at a Mach number of about 6.8. Generally, good agreement was obtained with both theory and data obtained in air except when the total angle (cone half-angle plus angle of attack) was great enough to promote nonconical flow. The center-of-pressure location was essentially constant within certain regions of angle of attack. Also, the normal-force and pitching-moment coefficients obtained in the present investigation were correlated with cone data at various bluntness ratios and Mach numbers.

## INTRODUCTION

The sharp right circular cone has traditionally been the subject of much theoretical and experimental research. Interest in this configuration has recently focused from a general viewpoint to a practical one as a result of suggestions that the simple cone might be attractive as an entry body at high velocities where the radiative heating characteristics of a configuration become important. Calculations in reference 1 show that the total heat entering certain sharp cones at speeds greater than twice the near-earth satellite velocity is less than 1 percent of the entry kinetic energy as a result of the low radiative heating properties of this configuration. Results of this reference also indicate that prohibitive radiative heating would result from the use of blunt configurations at similar velocities. Furthermore, the sharp cone has inherently desirable static-stability characteristics at hypersonic speeds. References 2 and 3 predict the center-of-pressure location to be rearward of the center of volume for a cone of semiapex angle similar to 19.5° and rearward of the cone base for a cone of semiapex angle similar to 35°. This characteristic could allow considerable leeway (depending on the design cone angle) in the placement of the body center-of-gravity position.

Many investigations have been conducted on the sharp cone at the lower hypersonic Mach numbers. (See, for example, refs. 4 to 10.) Only two of these references (refs. 4 and 5), however, obtained experimental force data over a sizable range of cone angle and angle of attack. Additional investigations (refs. 11 to 19) have been conducted on the sharp cone at the higher Mach numbers ($M \approx 20$); however, these investigations were usually confined to slender configurations at angles of attack less than $30^\circ$. The present investigation was initiated to extend the knowledge of the high Mach number aerodynamic characteristics of the sharp right circular cone to considerably larger cone angles and higher angles of attack.

Calculations of Newtonian theory, Cheng's cone theory, and exact theory were made and compared with various performance parameters. In addition, a correlation of the data of the present investigation with cone data of reference 15 for various bluntness ratios and Mach numbers was made by using the correlation parameters of the same reference. Comparisons between the results from the present investigation obtained in helium and existing data obtained in air were also made in order to assess the effects of testing sharp cones in a helium environment.

The present investigation was conducted on cones of half-angles from $5^\circ$ to $90^\circ$ for angles of attack to $110^\circ$. Tests were conducted at a Mach number of 20.3 and a Reynolds number of $0.37 \times 10^6$ per inch ($14.6 \times 10^6$ per meter).

## SYMBOLS

Measurements for this investigation were taken in the U.S. Customary System of Units. Equivalent values are indicated herein parenthetically in the International System (SI) in the interest of promoting use of this system in future NASA reports. Details concerning the use of SI, together with physical constants and conversion factors, are given in reference 20.

The results of the present investigation are referred to both the wind- and body-axis systems. (See fig. 1.) All pitching-moment-coefficient data are referred to a point located 0.667 percent of the body length rearward from the model nose and on the geometric center line unless otherwise specified. (See table I.)

$A$ base area

$a$ speed of sound, $\sqrt{\left(\frac{\partial p}{\partial \rho}\right)_s}$

$C_A$ axial-force coefficient, $\frac{\text{Axial force}}{qA}$

$C_D$ drag coefficient, $C_A \cos \alpha + C_N \sin \alpha$

$C_F$ average skin-friction coefficient

$C_L$ lift coefficient, $C_N \cos \alpha - C_A \sin \alpha$

$C_{L_\alpha}$ lift-curve slope through $\alpha = 0^\circ$, $\frac{\partial C_L}{\partial \alpha}$

$C_m$ pitching-moment coefficient, $\frac{\text{Pitching moment}}{qAd}$

$C_{m_\alpha}$ pitching-moment-curve slope through $\alpha = 0^\circ$, $\frac{\partial C_m}{\partial \alpha}$

$C_N$ normal-force coefficient, $\frac{\text{Normal force}}{qA}$

$C_{N_\alpha}$ normal-force-curve slope through $\alpha = 0^\circ$, $\frac{\partial C_N}{\partial \alpha}$

$C_p$ pressure coefficient

$d$ maximum body diameter

L/D lift-drag ratio

$l$ body length

$\bar{l}$ surface length

M Mach number

p pressure

q dynamic pressure

R Reynolds number

$\bar{R}$ gas constant

r radius of model base

T temperature

V velocity

$x_{cm}$ distance from model nose to moment reference location

$x_{cp}$ distance from model nose to center-of-pressure location

$\frac{x_{cp}}{l}$ center-of-pressure location for nonzero angle of attack, $\left(\frac{x_{cm}}{d} - \frac{C_m}{C_N}\right)\frac{d}{l}$

$\left(\frac{x_{cp}}{l}\right)_{\alpha=0^\circ}$ initial center-of-pressure location, $\left[\frac{x_{cm}}{d} - \left(\frac{\partial C_m}{\partial C_N}\right)_{\alpha=0^\circ}\right]\frac{d}{l}$

$$\frac{\bar{x}}{r} = (57.296)\left(\frac{2}{3\theta_c}\right)\left[\left(\frac{1 - \xi^3}{1 - \xi^2}\right) - \xi\left(\frac{1 - \theta_c}{\theta_c}\right)\right]$$

$\alpha$ angle of attack

$\alpha_m$ angle of attack for maximum lift coefficient or maximum lift-drag ratio

$\gamma$ specific-heat ratio

$\epsilon = \frac{\gamma - 1}{\gamma + 1}$

$\theta$ cone semivertex angle

$\kappa = \left(\frac{\gamma + 1}{\gamma - 1}\right)\frac{1}{\gamma M_\infty{}^2 \sin^2\theta_c}$

$\mu$ dynamic viscosity

$\xi$ nose bluntness ratio, $\frac{r_n}{r}$

$\rho$ density

Subscripts:

c cone surface conditions

max maximum

nose coefficient referred to model nose

s constant entropy

$\alpha=0^\circ$ parameter at zero angle of attack

$\infty$ free-stream conditions

## APPARATUS AND TESTS

### Models

Dimensions of the models used for each particular cone angle and angle of attack are given in table I, and the methods of attaching the model to the balance are illustrated in figure 2. All models were fabricated from aluminum and had their external surfaces highly polished.

### Tests

The investigation was conducted at a Mach number of 20.3 and a Reynolds number of $0.37 \times 10^6$ per inch $(14.6 \times 10^6$ per meter) in the contoured nozzle of the Langley 22-inch helium tunnel, a sketch of which is shown in figure 3. The pressure in the tunnel stagnation chamber was approximately 1015 lbf/sq in. abs (7 meganewtons/square meter) and the temperature was about $540^\circ$ R ($302^\circ$ Kelvin). A comprehensive calibration and description of this facility is presented in reference 12.

Several sting-mounted strain-gage balances were used to measure the longitudinal coefficients. The maximum inaccuracies in the coefficients as determined from a static-balance calibration are presented in table II, where the pitching-moment inaccuracies have been adjusted to include the error due to transferring moments from the balance pitch center to the moment reference position.

No base-pressure corrections were made to the data.

## THEORETICAL CALCULATIONS

The data obtained in the present investigation have been compared with Newtonian theoretical results obtained from the tabulated values of reference 2 for angles of attack from $1^\circ$ to $85^\circ$ and, where available, from the charts of reference 5 for angles of attack from $85^\circ$ to $110^\circ$. Calculations on the $15^\circ$ half-angle cone from $\alpha = 85^\circ$ to $\alpha = 95^\circ$ were made by using the method of reference 21 modified to account for the pitching moment due to axial force. All Newtonian calculations are based on a value of $C_{p,max}$ of 2.0.

The exact results for $C_{N_\alpha}$, $C_{l_\alpha}$, and $(C_A)_{\alpha=0^\circ}$ in air were obtained from reference 22, whereas the exact values for $(C_A)_{\alpha=0^\circ}$ in helium were obtained from reference 23. Values resulting from Cheng's cone theory (ref. 24) were computed by using the following equations:

$$C_{N_\alpha} = \frac{1}{57.296}\left[2\cos^2\theta_c + \epsilon\left(\frac{4}{15} - \frac{\sin\theta_c}{2}\right)\right]$$

$$(C_A)_{\alpha=0^\circ} = 2\sin\theta_c\left[1 + \frac{\epsilon}{4} + \frac{5\epsilon\kappa}{4} + \epsilon^2\left(\frac{\tan^2\theta_c}{4} + \frac{3}{32}\right)\right]$$

$$C_{L_\alpha} = C_{N_\alpha} - \frac{(C_A)_{\alpha=0^\circ}}{57.296}$$

An estimation of the average skin-friction coefficient has been computed by applying the T' method given by Monaghan in reference 25 to a sharp cone at adiabatic conditions. When $C_F$ was computed by this method, the Reynolds number on the cone surface was calculated and referred to the free-stream Reynolds number. The results of these calculations are presented in figure 4 for various hypersonic Mach numbers. The following equation was used to determine the ratio $R_c/R_\infty$:

$$\frac{R_c}{R_\infty} = \left(\frac{\rho_c V_c \bar{l}}{\mu_c}\right)\left(\frac{\mu_\infty}{\rho_\infty V_\infty \bar{l}}\right) = \left(\frac{\rho_c}{\rho_\infty}\right)\left(\frac{V_c}{V_\infty}\right)\left(\frac{\mu_c}{\mu_\infty}\right)^{-1}$$

Use of the viscosity equation for helium

$$\mu = 8.315T^{0.647} \times 10^{-4}$$

for $10^\circ$ R < T < $1300^\circ$ R ($6^\circ$ K < T < $722^\circ$ K) and the relation for a thermally perfect gas

$$V \equiv Ma = M\sqrt{\gamma \bar{R} T}$$

results in

$$\frac{R_c}{R_\infty} = \left(\frac{p_c}{p_\infty}\right)^{-0.147}\left(\frac{M_c}{M_\infty}\right)\left(\frac{\rho_\infty}{\rho_c}\right)^{-1.147}$$

Each of the values in the final equation for $R_c/R_\infty$ can be obtained from the charts in reference 23 for a given free-stream Mach number and $\gamma = \frac{5}{3}$. The skin-friction coefficient computed by this method was applied to the theoretical results (summary figs. only) for $(C_A)_{\alpha=0^\circ}$ $\left(\theta_c \leq 40^\circ\right)$ and $\left(\frac{L}{D}\right)_{max}$ $\left(\theta_c \leq 20^\circ\right)$, where the value of $C_F$ computed at $\alpha = 0^\circ$ was assumed to be invariant with angle of attack.

## RESULTS AND DISCUSSION

For the experimental portion of the investigation, the model base diameter had to be varied to accommodate the load ranges of the measuring equipment. The resulting change in Reynolds number was assumed to have little effect on the results of the tests, and, in fact, results of reference 5 at $M_\infty = 6.83$ showed that a fivefold increase in Reynolds number produced no change in the aerodynamic characteristics of a $5^\circ$ half-angle cone except for a decrease in drag due to reduced skin friction.

Basic data are presented in figure 5 (referred to body axes) and figure 6 (referred to wind axes), and the summary results are included in figures 7 to 13. Theoretical predictions and results obtained in air at $M_\infty \approx 6.8$ (ref. 4 and the data of ref. 5 for $\alpha = 0^\circ$ to $\alpha = 30^\circ$) are also included in these figures. The variations of the center-of-pressure location with cone semivertex angle and angle of attack are presented in figures 14 and 15, respectively, and the normal-force and pitching-moment coefficients are correlated with data from reference 15 in figures 16 and 17, respectively.

### Basic Data

Normal-force and pitching-moment coefficients are well predicted by theory for total stagnation-line flow-deflection angles $(\theta_c + \alpha)$ less than $50^\circ$ to $60^\circ$. (See fig. 5.) The anomalies in the pitching-moment data for total angles greater than $50^\circ$ were observed on cones and other bodies at lower Mach numbers in references 10 and 26 and were attributed to a subsonic flow field between the shock and the model. This explanation could also account for the irregularities in the results of the present study since the theory of reference 23 shows that subsonic flow occurs on the cone surface for cones of half-angle slightly greater than $48^\circ$ and since shock detachment occurs on cones of a semivertex angle similar to $52^\circ$ for the present test conditions.

Figure 6 shows the basic data referred to the wind axes. In general, agreement between theory and experiment is very good. Exceptions include the overprediction of $\left(\frac{L}{D}\right)_{max}$ for $\theta_c \leqq 20^\circ$ (which would be expected because skin friction has been neglected in the theoretical values) and the disagreement between the theoretical and experimental values of both lift and drag coefficients for $\theta_c \geqq 50^\circ$. The discrepancies between these two parameters and theory, however, are such that the lift-drag ratio is well predicted by the theory. It is also interesting to note the rapid increase in the lift-drag ratio which occurs for angles of attack slightly greater than $90^\circ$. (See figs. 6(f) and 6(g), for example.) This increase occurs because the lift coefficient is greatly increased by the flat model base while the drag coefficient remains relatively constant.

## Summary Characteristics

The variation of normal-force-curve slope with cone angle is shown in figure 7. The air data points for $\theta_c = 90^\circ$ in figures 7 and 8 were obtained from the circular wing of reference 27. Both the exact theory of reference 22 and Cheng's cone theory (ref. 24) offer good predictions of the experimental data in figure 7. Newtonian theory is also seen to provide a good prediction of the normal-force-curve slope except for the $50^\circ$ and $60^\circ$ cone angles, where there is considerable disagreement between the theory and the data obtained in helium. A possible reason for this disagreement is the onset of shock detachment for the helium data. Figure 8, which presents the variation of the lift-curve slope with cone angle, also shows this sharp divergence between the impact theory and the experimental helium values at high cone angles. For cones of half-angle greater than $45^\circ$, $C_{L_\alpha}$ is negative. This fact and the fact that a high initial drag coefficient is characteristic of large cone angles indicate that the dynamic stability may be adversely affected, inasmuch as the results of reference 28 indicated that for a reentry trajectory, both negative values of $C_{L_\alpha}$ and large values of $C_D$ are undesirable for dynamic stability.

The maximum lift coefficient (and the angle of attack at which it occurs) is shown in figure 9 and is seen to decrease rapidly with increasing cone angle and to approach zero as the cone semivertex angle nears $45^\circ$ (positive $C_{L,max}$). Newtonian theory adequately predicts the values of $C_{L,max}$ and $\alpha_m$ throughout the entire angle-of-attack range. The maximum lift-drag ratio with the corresponding angle of attack is shown in figure 10. The dashed curve in this figure was obtained by including the average skin-friction coefficient (computed for $\alpha = 0^\circ$, $\gamma = 5/3$, $M_\infty = 20.3$, and $R_\infty = 0.37 \times 10^6$ per in. ($14.6 \times 10^6$ per meter)) in the calculations for $\left(\frac{L}{D}\right)_{max}$.

Figure 11(a) presents a plot of the lift coefficient at the angle of attack for $\left(\frac{L}{D}\right)_{max}$ as a function of cone angle. From the helium data and the theory included in this figure, it is seen that the maximum value of lift coefficient at $\left(\frac{L}{D}\right)_{max}$ occurs at $\theta_c \approx 20^\circ$. The lift-drag ratio at the angle of attack for maximum lift coefficient is shown in figure 11(b) as a function of cone angle. The point plotted for $\theta_c = 0^\circ$ was obtained from a circular cylinder of reference 29. For positive values of L/D at $C_{L,max}$, Newtonian theory overpredicts the helium data for all cases. Except for the $\theta_c = 50^\circ$ cone, reasonable theoretical prediction of negative coefficients is shown in this figure. Figure 12, which presents the axial-force coefficient at $\alpha = 0^\circ$ as a function of cone angle, generally shows good agreement between the experimental results and the various theories, the exception being the cone of $5^\circ$ semivertex angle. It should be noted that between the cone semivertex angles of $50^\circ$ and $60^\circ$, a crossover from theory underprediction to overprediction occurs in the plot for $(C_A)_{\alpha=0^\circ}$. The crossover probably results from the shock detachment which occurs between these two angles and which Newtonian theory does not consider. For this figure, the skin-friction calculations were again computed for the helium test conditions.

Figure 13 presents the variation of the pitching-moment-curve slope with cone angle. Newtonian theory predicts this parameter for cone angles less than 50°.

## Center-of-Pressure Location

The initial center-of-pressure location $\left(\text{determined by measuring the slope } \frac{\partial C_m}{\partial C_N} \text{ through } \alpha = 0^\circ \text{ and referring to the model nose}\right)$ is shown in figure 14 where good agreement is obtained with theory for semivertex angles less than 50°. In figure 15, the center-of-pressure locations of the various cones are plotted as a function of angle of attack. Although these locations are well predicted by Newtonian theory and are essentially constant over a wide range of angle of attack for the 10°, 15°, and 20° half-angle cones, noticeable variations begin to occur at $\alpha \approx 35^\circ$. For $\theta_c \geqq 30^\circ$, the center-of-pressure position is constant only for small increments in angle of attack and significant changes occur as the angle of attack is increased. These variations are particularly evident for $\theta_c = 50^\circ$ and $\theta_c = 60^\circ$. The effect that such test errors as sting size, base pressure, and model-balance orientation have on this sensitive parameter is not known.

One further point worth noting in this figure is the Newtonian prediction that the center-of-pressure position of the blunter cones would lie rearward of the model base. The prediction is seen to be verified when $\theta_c \geqq 40^\circ$ not only at $\alpha = 0^\circ$ (as evident in fig. 14) but throughout the entire angle-of-attack range. Thus, from the standpoint of this design consideration, the pointed cone with a semiapex angle greater than or equal to 40° appears to be a desirable reentry body.

## Correlation of Normal-Force Coefficients and Pitching-Moment Coefficients

Correlation parameters from reference 15 were applied to the data of the present investigation. The normal-force-coefficient correlation parameter along with the data of the present investigation and the data of reference 15 (for $\gamma = 7/5$) for various bluntness ratios and Mach numbers is presented in figure 16. This correlating parameter becomes less valid with increasing cone angle, until for $\theta_c \geqq 50^\circ$ no correlation is obtained. The inset in this figure illustrates the maximum angle of attack for which data on a given cone fall on the correlation curve.

The correlation parameter for the pitching-moment coefficient (referred to the model nose) is shown in figure 17. In this figure, the data obtained in helium represent values taken at approximately 10° increments in angle of attack. The good correlation evident in this figure is especially significant since the maximum angle of attack for most of the helium coefficients approached 110°. In addition, for a given cone, values of $C_{m,nose}$ obtained at angles of

attack greater than that for $C_{N,max}$ (indicated by flagged symbols) correlate with values of $C_{m,nose}$ obtained at angles of attack less than that for $C_{N,max}$. It should be noted that, with increasing cone angle, the pitching-moment coefficients diverge slightly from the correlation line of reference 15; however, this divergence is nearly constant for $20^\circ \leqq \theta_c \leqq 50^\circ$. For the cone with a $60^\circ$ semivertex angle, relatively poor correlation is obtained.

The results of the present investigation extend the range of applicability of the correlation parameters to much higher cone angles than those of reference 15 and also indicate the degree of correlation to be expected as a function of cone angle. The correlation for $\theta_c \geqq 20^\circ$ obtained with these parameters is somewhat surprising since they were originally derived for slender conical configurations.

## Air-Helium Comparison

References 30 and 31 have theoretically treated the problem of converting results obtained in a helium environment to equivalent values in air, whereas references 11, 13, 16, and 32 to 37 have studied it experimentally to varying degrees. Inasmuch as comparisons of air and helium data provide a direct method of determining specific-heat-ratio effects, the present helium data are compared with the available air data of references 4 and 5 whenever possible. Differences in the values of $C_{p,max}$ obtained in helium and air would, of course, affect these comparisons ($C_{p,max} = 1.815$ in air and 1.748 in helium). Values of $C_{p,max}$ were computed by using the following equation presented in reference 38:

$$C_{p,max} = \left(\frac{\gamma + 3}{\gamma + 1}\right)\left[1 - \frac{2}{(\gamma + 3)M_\infty^2}\right]$$

Small discrepancies in the normal-force and pitching-moment coefficients occur between the air and helium data when $(\theta_c + \alpha) > 50^\circ$. These discrepancies are particularly evident in the data for the $50^\circ$ half-angle cone (fig. 5(g)), for which angle there exists a considerable difference in the character of the air and helium flow fields. This difference can be seen from the theory of references 39 and 23; the theory of reference 39 shows a completely supersonic flow downstream of the shock wave for the cone in air, whereas that of reference 23 for the cone in helium reveals a subsonic compressible flow on the surface of the cone. The difference in flow fields between the air and helium data is a result of the difference in the specific-heat ratios rather than the difference in Mach numbers. This explanation would also account for the considerable difference between the air and helium values of $C_{N_\alpha}$ and $C_{l_\alpha}$ obtained with the $50^\circ$ cone. (See figs. 7 and 8.)

A likely explanation for the fair Newtonian prediction of the initial normal-force and pitching-moment coefficients for the $50^\circ$ cone in air and the poorer prediction for the cone in helium (fig. 5(g)) is contained in the Newtonian assumption that the shock lies close to the body. This condition is seen to be violated by the theoretical values given in references 39 and 23, which show that for the $50^\circ$ semivertex-angle cone in air at $M_\infty = 6.8$, the shock-wave angle is approximately $59.4^\circ$ (ref. 39), whereas for the same cone in

helium at $M = 20.3$ the shock-wave angle is approximately $66.6^\circ$ (ref. 23). In contrast, for a cone of semivertex angle of $40^\circ$, the difference in shock-wave angle between the two test mediums is only about $2^\circ$ and both the initial normal-force and pitching-moment coefficient data agree very well with theory.

The earlier observation (see Basic Data section) that the helium pitching-moment coefficients departed from the Newtonian prediction when $(\theta_c + \alpha) > 50^\circ$ can also be seen in the air data of figures 5(e) to 5(g). The departure occurs at a slightly higher angle of attack, however, because the shock detachment angle of the air data is greater than that of the helium data.

Some additional effects of using helium rather than air as the test gas are the smaller maximum values of the normal-force coefficient (apparent, for example, on the $20^\circ$ half-angle cone of figure 5(d)) and the higher values for $C_A$ on the $15^\circ$ and $30^\circ$ semivertex-angle cones at angles of attack greater than $75^\circ$ (figs. 5(c) and 5(e)).

A considerable difference is also evident between the air and helium predictions of Cheng's cone theory for $(C_A)_{\alpha=0^\circ}$. (See fig. 12.) This difference is primarily due to the large difference in Mach number (rather than specific-heat ratio) between the air and helium predictions, but its magnitude decreases significantly with increasing cone angle.

Except for these discrepancies between the air and helium data, there is generally good agreement between the data of the present investigation and the data of references 4 and 5 obtained in air.

## CONCLUDING REMARKS

The static aerodynamic characteristics of a family of sharp right circular cones ranging in half-angle from $5^\circ$ to $90^\circ$ have been obtained for angles of attack to $110^\circ$ at a Mach number of 20.3 in helium. The data have been compared with Newtonian theory, Cheng's cone theory, exact theory, and existing data obtained in air at a Mach number of 6.8. In general, good agreement was obtained with both theory and air data except when the total angle (cone semivertex angle plus angle of attack) was large enough to promote nonconical flow.

In addition, the sharp-cone data of this investigation have been correlated with cone data at various bluntness ratios and Mach numbers by means of correlation parameters for normal-force and pitching-moment coefficients. The normal-force-coefficient parameter proved to have considerably less correlating ability as the cone half-angle was increased; however, good correlation was obtained with the pitching-moment-coefficient parameter for cones of half-angle less than $50^\circ$.

Langley Research Center,
National Aeronautics and Space Administration,
Langley Station, Hampton, Va., August 27, 1965.

## REFERENCES


1. Seiff, Alvin: Developments in Entry Vehicle Technology. AIAA Paper No. 64-528, Am. Inst. Aeron. Astronaut., July 1964.

2. Wells, William R.; and Armstrong, William O.: Tables of Aerodynamic Coefficients Obtained From Developed Newtonian Expressions for Complete and Partial Conic and Spheric Bodies at Combined Angles of Attack and Sideslip With Some Comparisons With Hypersonic Experimental Data. NASA TR R-127, 1962.

3. Charwat, A. F.: The Stability of Bodies of Revolution at Very High Mach Numbers. Jet Propulsion, vol. 27, no. 8, pt. 1, Aug. 1957, pp. 866-871.

4. Penland, Jim A.: Aerodynamic Force Characteristics of a Series of Lifting Cone and Cone-Cylinder Configurations at a Mach Number of 6.83 and Angles of Attack up to 130°. NASA TN D-840, 1961.

5. Penland, Jim A.: A Study of the Stability and Location of the Center of Pressure on Sharp, Right Circular Cones at Hypersonic Speeds. NASA TN D-2283, 1964.

6. Shantz, I.: Cone Static Stability Investigation at Mach Numbers 1.56 Through 4.24. NAVORD Rept. 3584, U.S. Naval Ord. Lab. (White Oak, Md.), Dec. 7, 1953. (Available as ASTIA Doc. AD 128203.)

7. Oliver, Robert E.: An Experimental Investigation of Flow Over Simple Blunt Bodies at a Nominal Mach Number of 5.8. GALCIT Memo. No. 26 (Contract No. DA-04-495-Ord-19), June 1, 1955.

8. Dennis, David H.; and Cunningham, Bernard E.: Forces and Moments on Pointed and Blunt-Nosed Bodies of Revolution at Mach Numbers From 2.75 to 5.00. NACA RM A52E22, 1952.

9. Peckham, D. H.: Experiments at Hypersonic Speeds on Circular Cones at Incidence. Tech. Note No. Aero. 2863, Brit. R.A.E., Jan. 1963.

10. Neal, Luther, Jr.: Aerodynamic Characteristics at a Mach Number of 6.77 of a 9° Cone Configuration, With and Without Spherical Afterbodies, at Angles of Attack up to 180° With Various Degrees of Nose Blunting. NASA TN D-1606, 1963.

11. Arrington, James P.; and Maddalon, Dal V.: Aerodynamic Characteristics of Several Lifting and Nonlifting Configurations at Hypersonic Speeds in Air and Helium. NASA TM X-918, 1964.

12. Arrington, James P.; Joiner, Roy C., Jr.; and Henderson, Arthur, Jr.: Longitudinal Characteristics of Several Configurations at Hypersonic Mach Numbers in Conical and Contoured Nozzles. NASA TN D-2489, 1964.

13. Henderson, Arthur, Jr.: Recent Investigations of the Aerodynamic Characteristics of General and Specific Lifting and Nonlifting Configurations at Mach 24 in Helium, Including Air-Helium Simulation Studies. The High Temperature Aspects of Hypersonic Flow, Wilbur C. Nelson, ed., AGARDograph 68, Pergamon Press, 1964, pp. 163-190.

14. Witcofski, Robert D.; and Woods, William C.: Static Stability Characteristics of Blunt Low-Fineness-Ratio Bodies of Revolution at a Mach Number of 24.5 in Helium. NASA TN D-2282, 1964.

15. Whitfield, Jack D.; and Wolny, W.: Hypersonic Static Stability of Blunt Slender Cones. AEDC-TDR-62-166 (Contract No. AF 40(600)-1000), Arnold Eng. Dev. Center, Aug. 1962.

16. Ladson, Charles L.; and Blackstock, Thomas A. (With appendix by Donald L. Baradell and Thomas A. Blackstock): Air-Helium Simulation of the Aerodynamic Force Coefficients of Cones at Hypersonic Speeds. NASA TN D-1473, 1962.

17. Short, Barbara J.; Whiting, Ellis E.; Kruse, Robert L.; and Malcolm, Gerald N.: A Comparison of the Hypersonic Static Stability Characteristics of Blunt- and Pointed-Nosed Slender Entry Vehicles. NASA TM X-850, 1963.

18. Intrieri, Peter F.: Study of the Stability and Drag at Mach Numbers From 4.5 to 13.5 of a Conical Venus-Entry Body. NASA TN D-2827, 1965.

19. Whitfield, Jack D.; and Griffith, B. J.: Viscous Effects on Zero-Lift Drag of Slender Blunt Cones. AEDC-TDR-63-35, U.S. Air Force, Mar. 1963.

20. Mechtly, E. A.: The International System of Units - Physical Constants and Conversion Factors. NASA SP-7012, 1964.

21. Rainey, Robert W.: Working Charts for Rapid Prediction of Force and Pressure Coefficients on Arbitrary Bodies of Revolution by Use of Newtonian Concepts. NASA TN D-176, 1959.

22. Bertram, Mitchel H.: Correlation Graphs for Supersonic Flow Around Right Circular Cones at Zero Yaw in Air as a Perfect Gas. NASA TN D-2339, 1964.

23. Henderson, Arthur, Jr.; and Braswell, Dorothy O.: Charts for Conical and Two-Dimensional Oblique-Shock Flow Parameters in Helium at Mach Numbers From About 1 to 100. NASA TN D-819, 1961.

24. Cheng, Hsien K.: Hypersonic Shock-Layer Theory of a Yawed Cone and Other Three-Dimensional Pointed Bodies. WADC TN 59-335, U.S. Air Force, Oct. 1959; Errata, June 1960.

25. Monaghan, R. J.: An Approximate Solution of the Compressible Laminar Boundary Layer on a Flat Plate. R. & M. No. 2760, British A.R.C., 1953.

26. Fetterman, David E.; and Neal, Luther, Jr.: An Analysis of the Delta-Wing Hypersonic Stability and Control Behavior at Angles of Attack Between 30° and 90°. NASA TN D-1602, 1963.

27. Penland, Jim A.; and Armstrong, William O.: Static Longitudinal Aerodynamic Characteristics of Several Wing and Blunt-Body Shapes Applicable for Use as Reentry Configurations at a Mach Number of 6.8 and Angles of Attack up to 90°. NASA TM X-65, 1959.

28. Allen, H. Julian: Motion of a Ballistic Missile Angularly Misalined With the Flight Path Upon Entering the Atmosphere and Its Effect Upon Aerodynamic Heating, Aerodynamic Loads, and Miss Distance. NACA TN 4048, 1957. (Supersedes NACA RM A56F15.)

29. Penland, Jim A.: Aerodynamic Characteristics of a Circular Cylinder at Mach Number 6.86 and Angles of Attack up to 90°. NACA TN 3861, 1957. (Supersedes NACA RM L54A14.)

30. Mueller, James N.: Conversion of Inviscid Normal-Force Coefficients in Helium to Equivalent Coefficients in Air for Simple Shapes at Hypersonic Speeds. NACA TN 3807, 1956.

31. Love, Eugene S.; Henderson, Arthur, Jr.; and Bertram, Mitchel H.: Some Aspects of Air-Helium Simulation and Hypersonic Approximations. NASA TN D-49, 1959.

32. Ladson, Charles L.: Effects of Several Nose and Vertical-Fin Modifications on the Low-Angle-of-Attack Static Stability of a Winged Reentry Vehicle at Mach Numbers of 9.6 in Air and 17.8 in Helium. NASA TM X-608, 1961.

33. Johnston, Patrick J.; and Snyder, Curtis D.: Static Longitudinal Stability and Performance of Several Ballistic Spacecraft Configurations in Helium at a Mach Number of 24.5. NASA TN D-1379, 1962.

34. Ladson, Charles L.: A Comparison of Aerodynamic Data Obtained in Air and Helium in the Langley 11-Inch Hypersonic Tunnel. NASA TM X-666, 1962.

35. Johnston, Patrick J.: Longitudinal Aerodynamic Characteristics of Several Fifth-Stage Scout Reentry Vehicles From Mach Number 0.60 to 24.4 Including Some Reynolds Number Effects on Stability at Hypersonic Speeds. NASA TN D-1638, 1963.

36. Harris, Julius E.: Force-Coefficient and Moment-Coefficient Correlations and Air-Helium Simulation for Spherically Blunted Cones. NASA TN D-2184, 1964.

37. Blackstock, Thomas A.; and Ladson, Charles L.: Comparison of the Hypersonic Aerodynamic Characteristics of Some Simple Winged Shapes in Air and Helium. NASA TN D-2328, 1964.

38. Lees, Lester: Hypersonic Flow. Fifth Intern. Aeron. Conf. (Los Angeles, Calif.), Inst. Aeron. Sci., Inc., June 1955, pp. 241-276.

39. Ames Research Staff: Equations, Tables, and Charts for Compressible Flow. NACA Rept. 1135, 1953. (Supersedes NACA TN 1428.)

TABLE I.- DIMENSIONS OF SHARP RIGHT CIRCULAR CONES

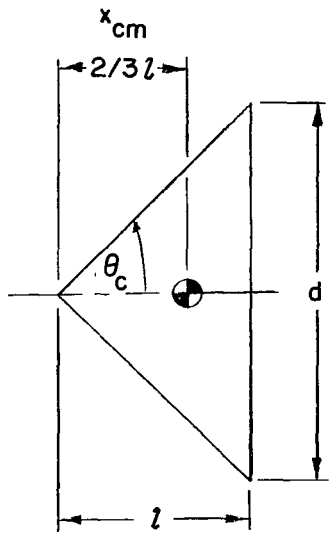


$\theta_c$=5° to 60°

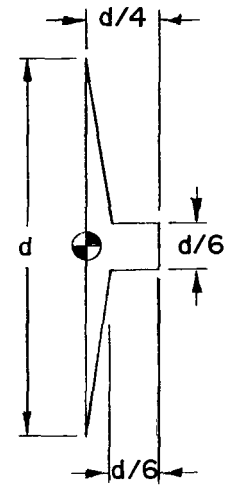


$\theta_c$=90°

| $\theta_c$, deg | $\alpha$, deg | d | | $l$ | | A | |
|---|---|---|---|---|---|---|---|
| | | in. | cm | in. | cm | sq in. | sq cm |
| 5 | 0 to 30 | 1.997 | 5.072 | 11.429 | 29.030 | 3.130 | 20.194 |
| 5 | 20 to 60 | 1.000 | 2.540 | 5.710 | 14.503 | .785 | 5.065 |
| 10 | 0 to 30 | 2.040 | 5.182 | 5.668 | 14.397 | 3.268 | 21.084 |
| 10 | 20 to 60 | 1.500 | 3.810 | 4.234 | 10.754 | 1.767 | 11.400 |
| 15 | 0 to 30 | 2.008 | 5.100 | 3.729 | 9.472 | 3.168 | 20.439 |
| 15 | 20 to 60 | 1.750 | 4.445 | 3.264 | 8.291 | 2.405 | 15.516 |
| 15 | 59 to 95 | 2.000 | 5.080 | 3.770 | 9.576 | 3.142 | 20.271 |
| 20 | 0 to 20 | 1.999 | 5.077 | 2.747 | 6.977 | 3.140 | 20.258 |
| 20 | 20 to 60 | 2.000 | 5.080 | 2.747 | 6.977 | 3.142 | 20.271 |
| 20 | 70 to 110 | 1.252 | 3.180 | 1.719 | 4.366 | 1.227 | 7.916 |
| 30 | 0 to 20 | 2.000 | 5.080 | 1.739 | 4.417 | 3.142 | 20.271 |
| 30 | 20 to 60 | 2.000 | 5.080 | 1.739 | 4.417 | 3.142 | 20.271 |
| 30 | 70 to 110 | 1.504 | 3.820 | 1.301 | 3.305 | 1.767 | 11.400 |
| 40 | 0 to 20 | 2.003 | 5.088 | 1.193 | 3.030 | 3.142 | 20.271 |
| 40 | 20 to 60 | 2.000 | 5.080 | 1.193 | 3.030 | 3.142 | 20.271 |
| 40 | 70 to 110 | 1.750 | 4.445 | 1.039 | 2.639 | 2.405 | 15.516 |
| 50 | 0 to 20 | 2.002 | 5.085 | .840 | 2.134 | 3.142 | 20.271 |
| 50 | 20 to 60 | 2.000 | 5.080 | .840 | 2.134 | 3.142 | 20.271 |
| 50 | 70 to 110 | 3.000 | 7.620 | 1.260 | 3.200 | 7.069 | 45.606 |
| 60 | 0 to 20 | 1.749 | 4.442 | .508 | 1.290 | 2.405 | 15.516 |
| 60 | 20 to 60 | 1.750 | 4.445 | .508 | 1.290 | 2.405 | 15.516 |
| 90 | 0 to 20 | 3.000 | 7.620 | 0 | 0 | 7.069 | 45.606 |

TABLE II.- ACCURACY OF AERODYNAMIC COEFFICIENTS

| $\theta_c$, deg | $\alpha$, deg | Accuracy of - | | |
|---|---|---|---|---|
| | | $C_N$ | $C_A$ | $C_m$ |
| 5 | 0 to 30 | ±0.006 | ±0.002 | ±0.004 |
| 5 | 20 to 60 | ±.049 | ±.016 | ------ |
| 10 | 0 to 30 | ±.006 | ±.002 | ±.002 |
| 10 | 20 to 60 | ±.022 | ±.007 | ±.008 |
| 15 | 0 to 30 | ±.006 | ±.002 | ±.002 |
| 15 | 20 to 60 | ±.016 | ±.005 | ±.005 |
| 15 | 59 to 95 | ±.010 | ±.010 | ±.006 |
| 20 | 0 to 20 | ±.006 | ±.006 | ±.001 |
| 20 | 20 to 60 | ±.012 | ±.004 | ±.004 |
| 20 | 70 to 110 | ±.015 | ±.015 | ±.009 |
| 30 | 0 to 20 | ±.006 | ±.006 | ±.001 |
| 30 | 20 to 60 | ±.012 | ±.004 | ±.004 |
| 30 | 70 to 110 | ±.011 | ±.011 | ±.007 |
| 40 | 0 to 20 | ±.006 | ±.006 | ±.002 |
| 40 | 20 to 60 | ±.012 | ±.004 | ±.006 |
| 40 | 70 to 110 | ±.008 | ±.008 | ±.004 |
| 50 | 0 to 20 | ±.006 | ±.006 | ±.003 |
| 50 | 20 to 60 | ±.012 | ±.004 | ±.007 |
| 50 | 70 to 110 | ±.001 | ±.002 | ±.001 |
| 60 | 0 to 20 | ±.008 | ±.008 | ±.005 |
| 60 | 20 to 60 | ±.016 | ±.005 | ±.012 |
| 90 | 0 to 20 | ±.004 | ±.013 | ±.004 |

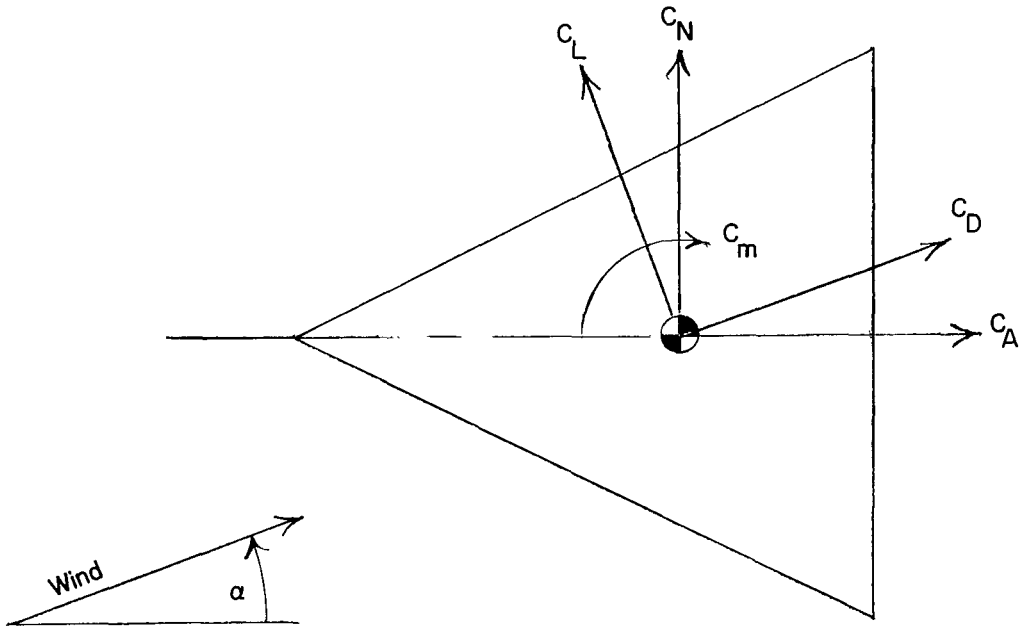


Figure 1.- Axis systems used. Arrows indicate positive direction.

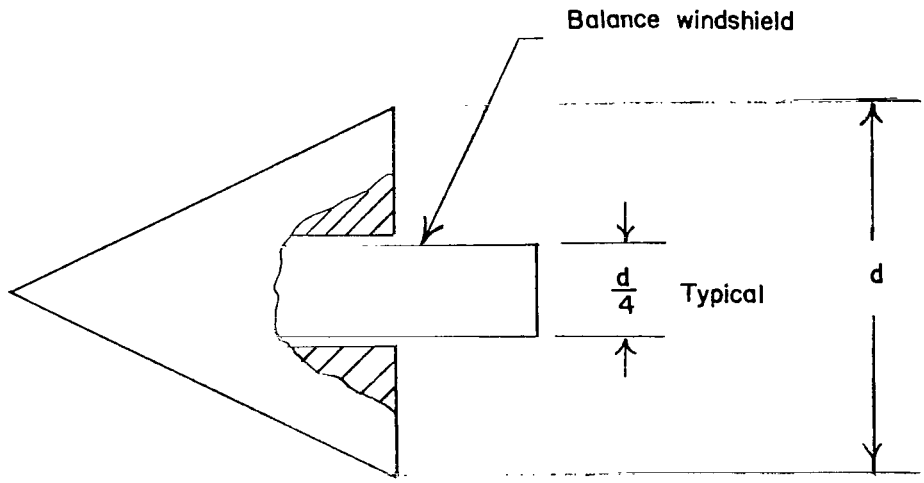


(a) $\alpha = 0^0$ to $60^0$.

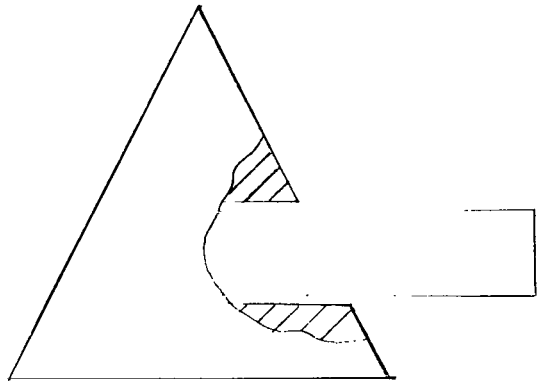

(b) $\alpha = 70^0$ to $110^0$.

Figure 2.- Model-balance mount arrangement.

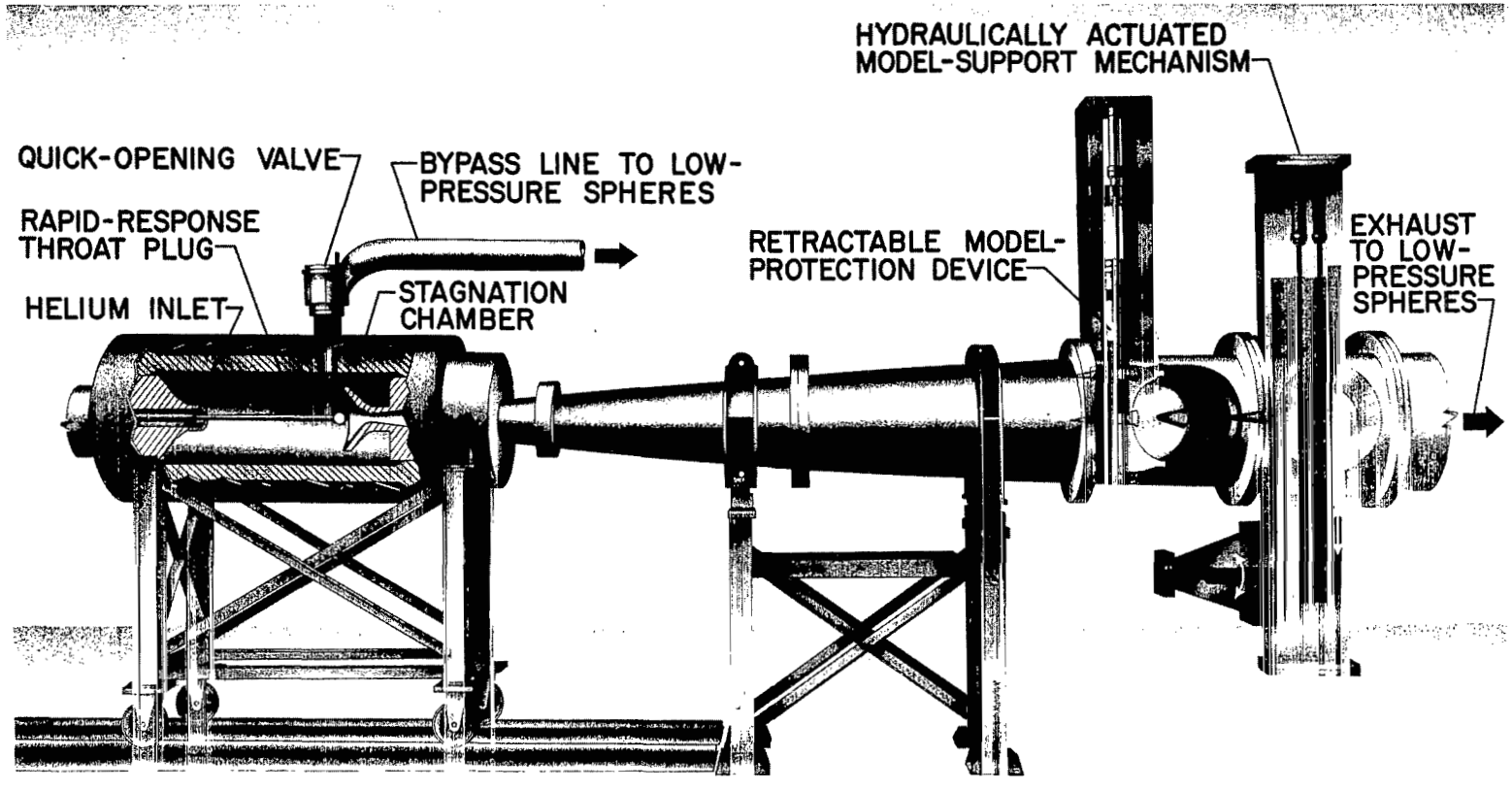


Figure 3.- Langley 22-inch helium tunnel with contoured nozzle.

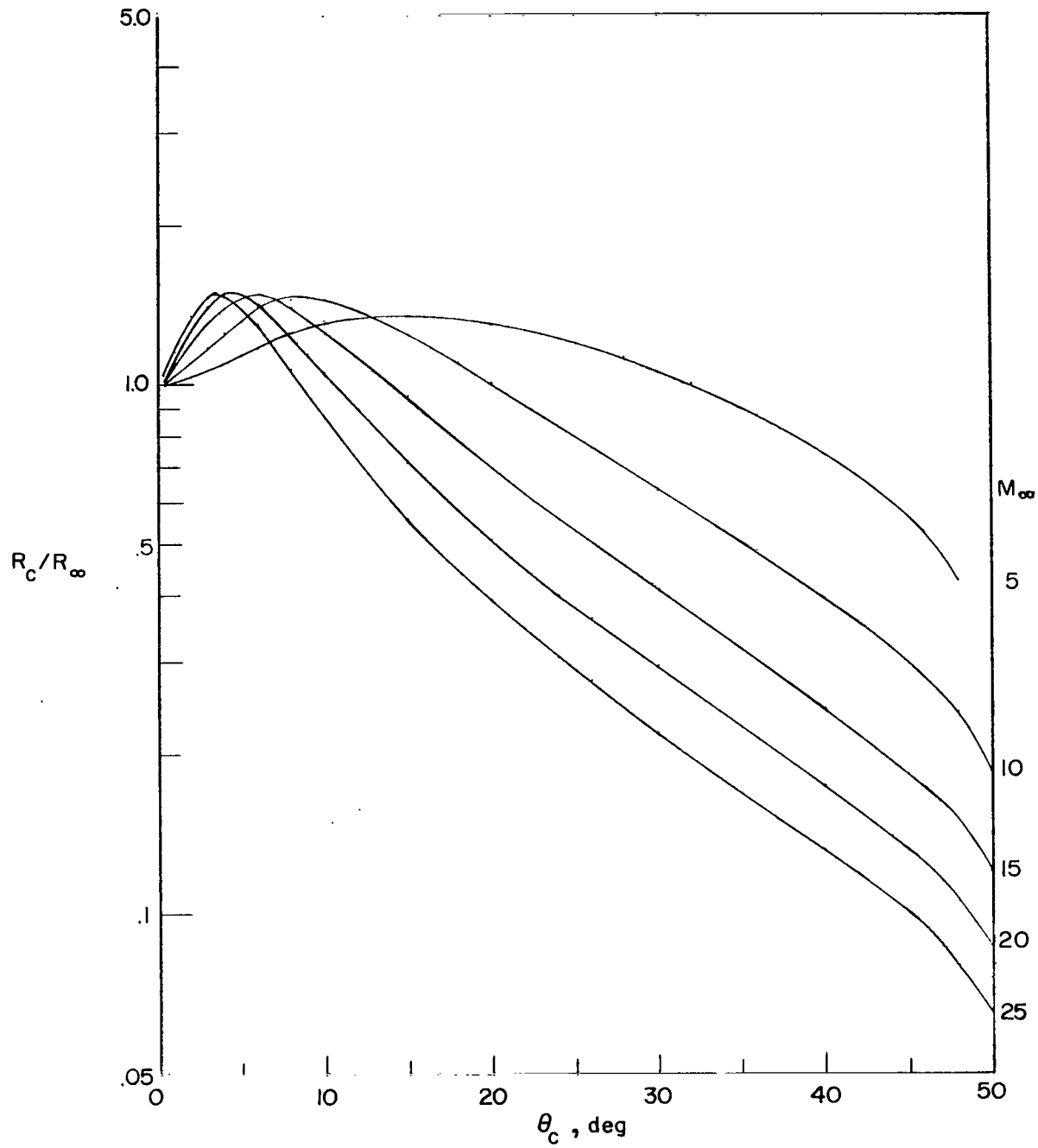


Figure 4.- Ratio of cone-surface Reynolds number to free-stream Reynolds number for helium plotted as a function of cone angle.

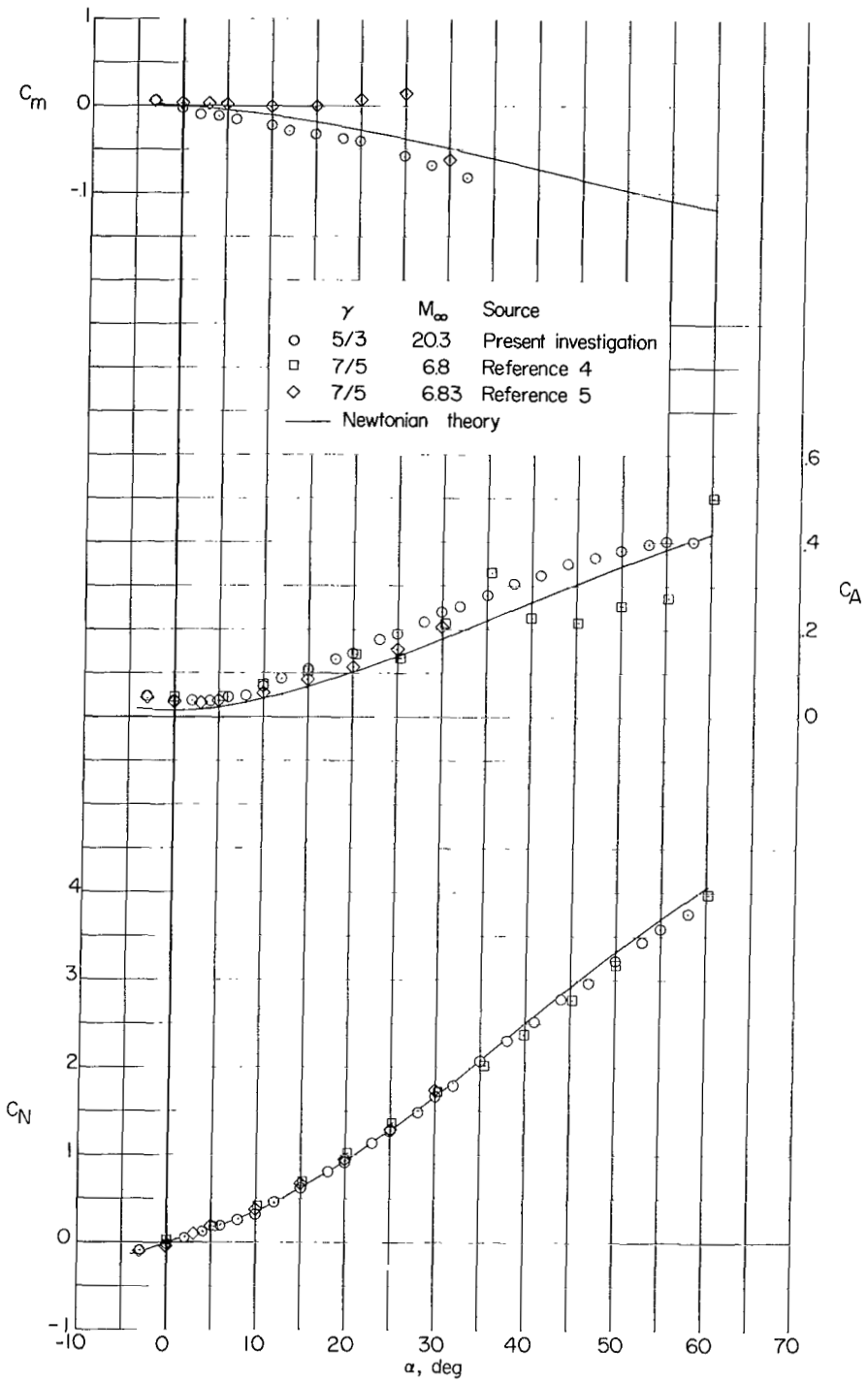


(a) $\theta_c = 5^0$.

Figure 5.- Longitudinal characteristics of sharp right circular cones referred to body-axis system in air and helium.

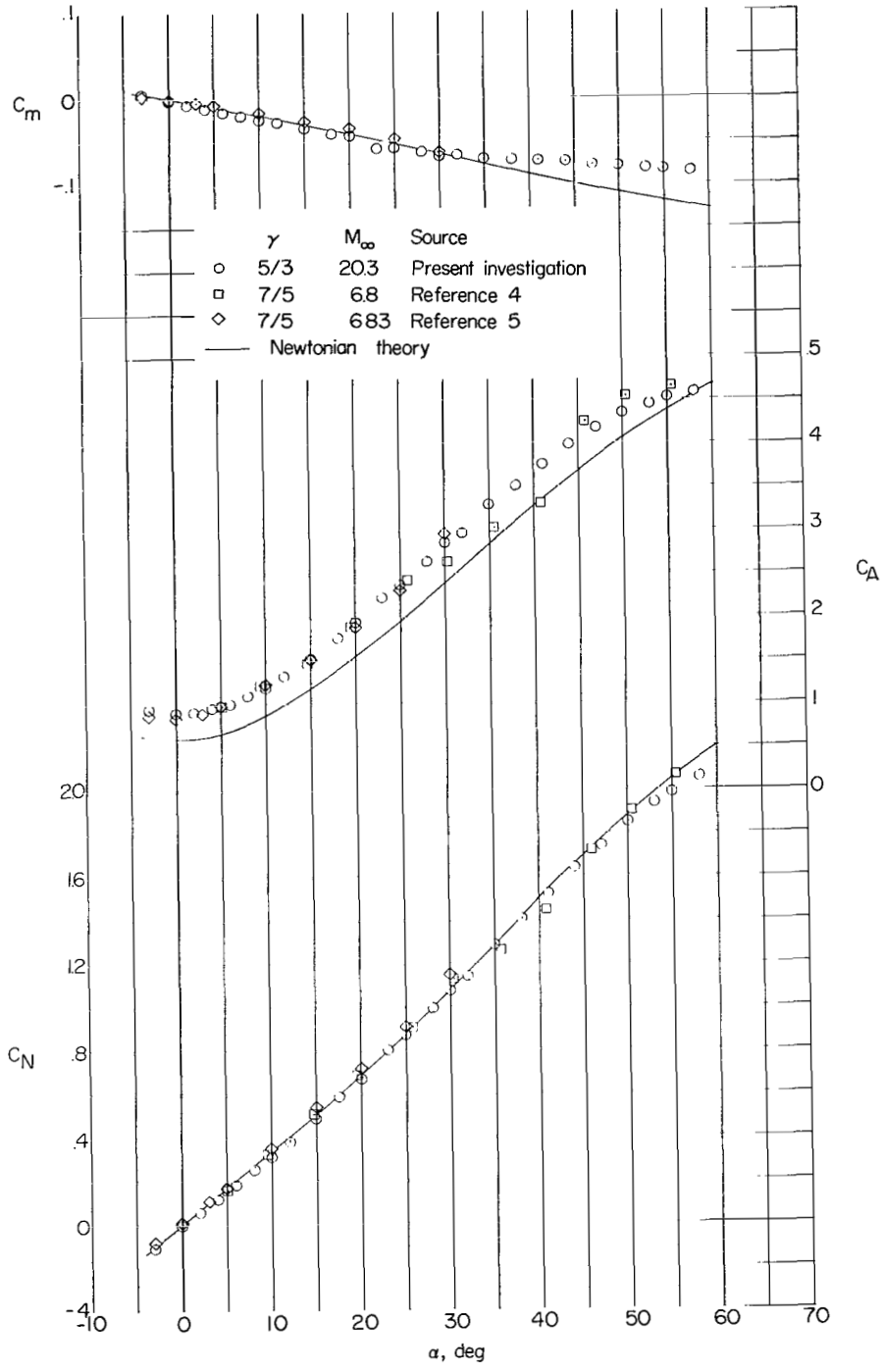


(b) $\theta_c = 10^0$.

Figure 5.- Continued.

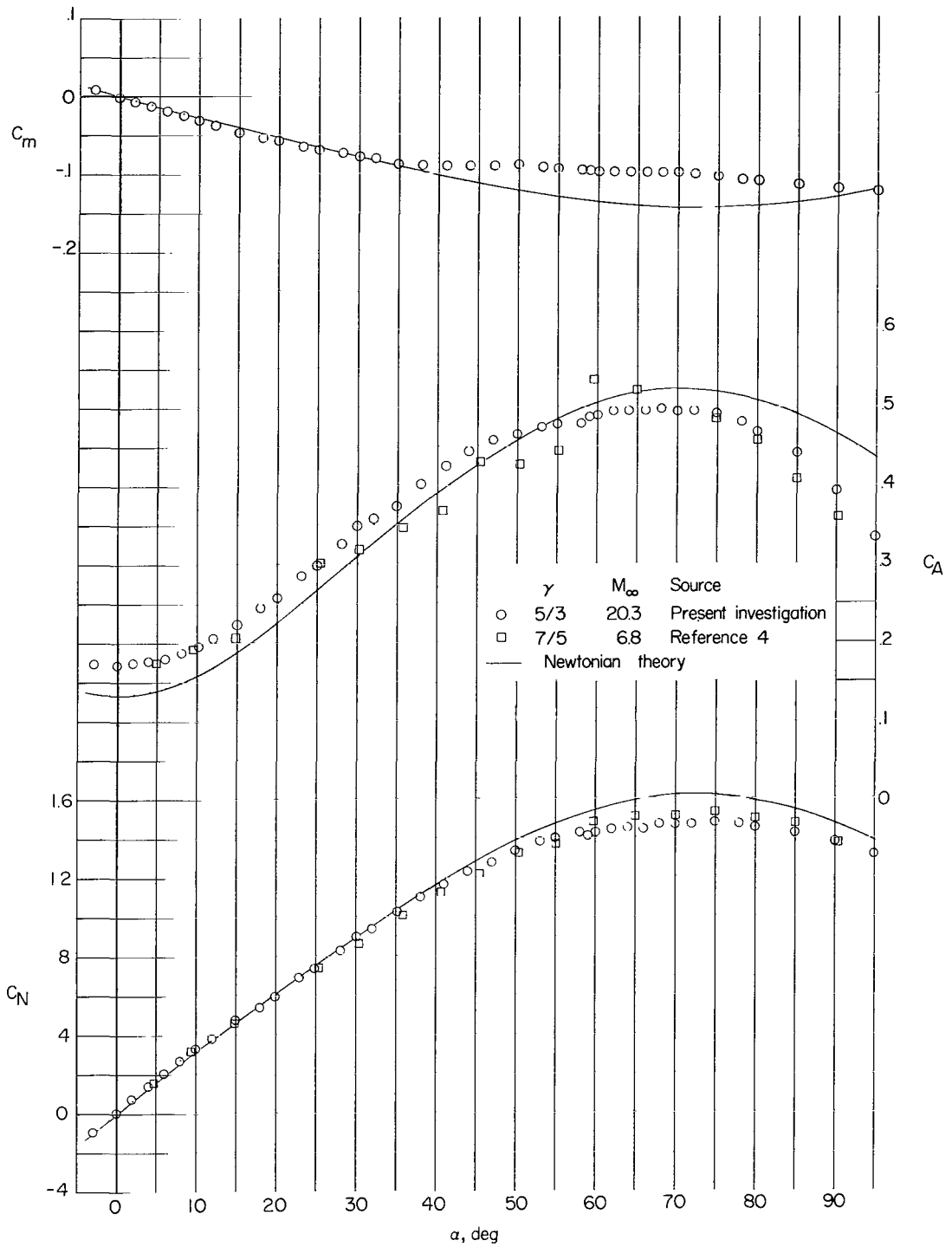


(c) $\theta_c = 15^0$.

Figure 5.- Continued.

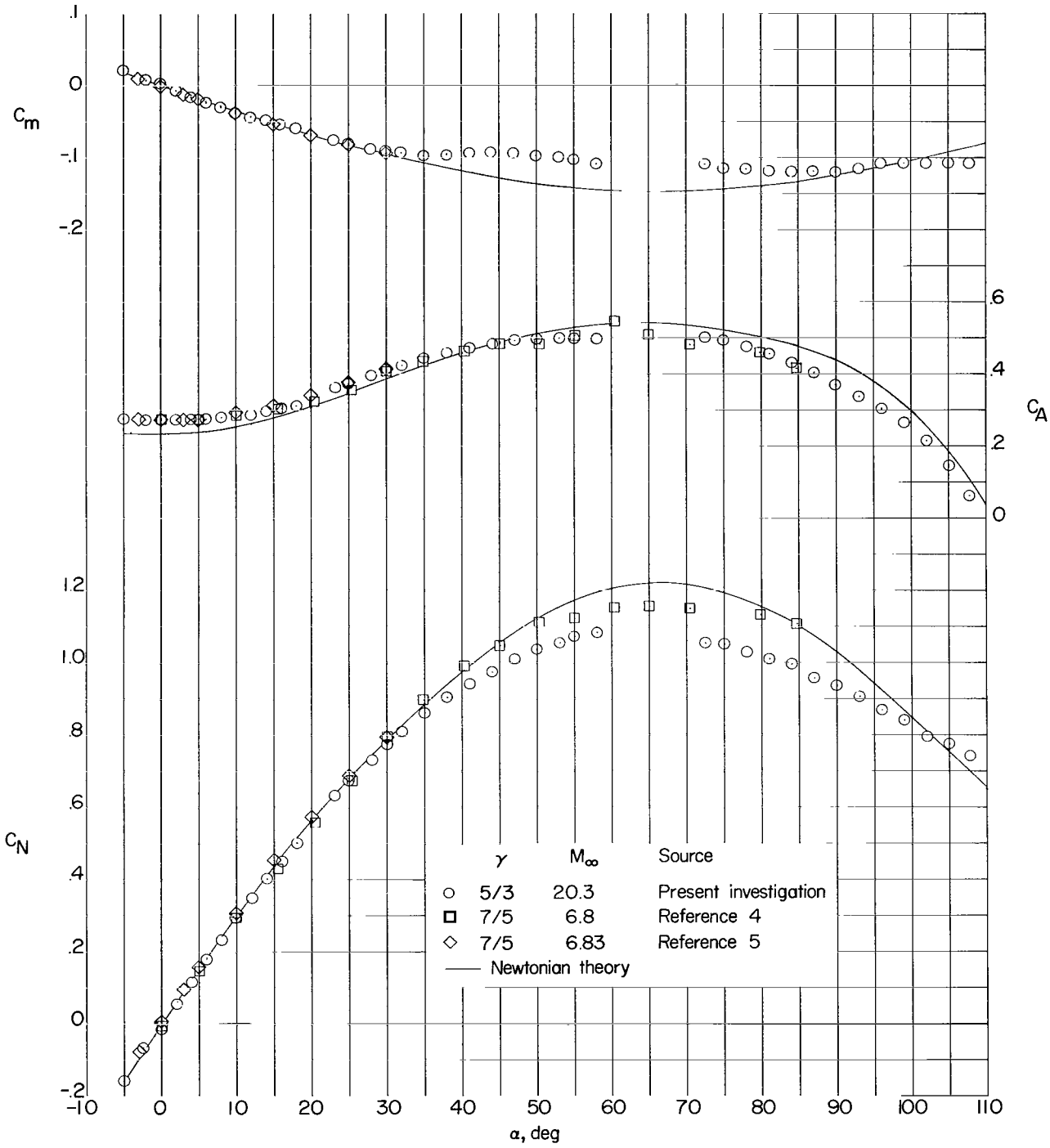


(d) $\theta_c = 20^0$.

Figure 5.- Continued.

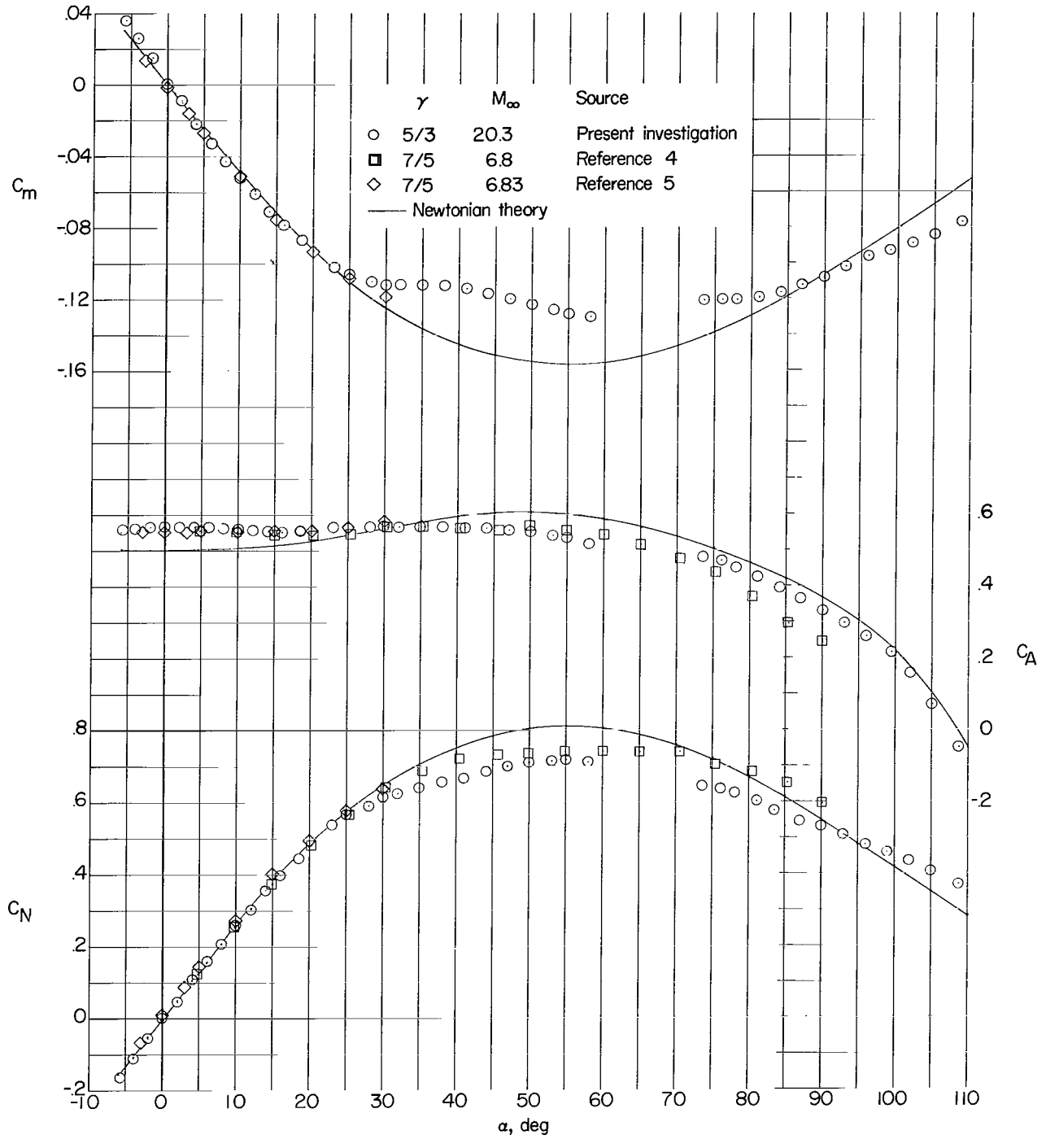


(e) $\theta_c = 30^0$.

Figure 5.- Continued.

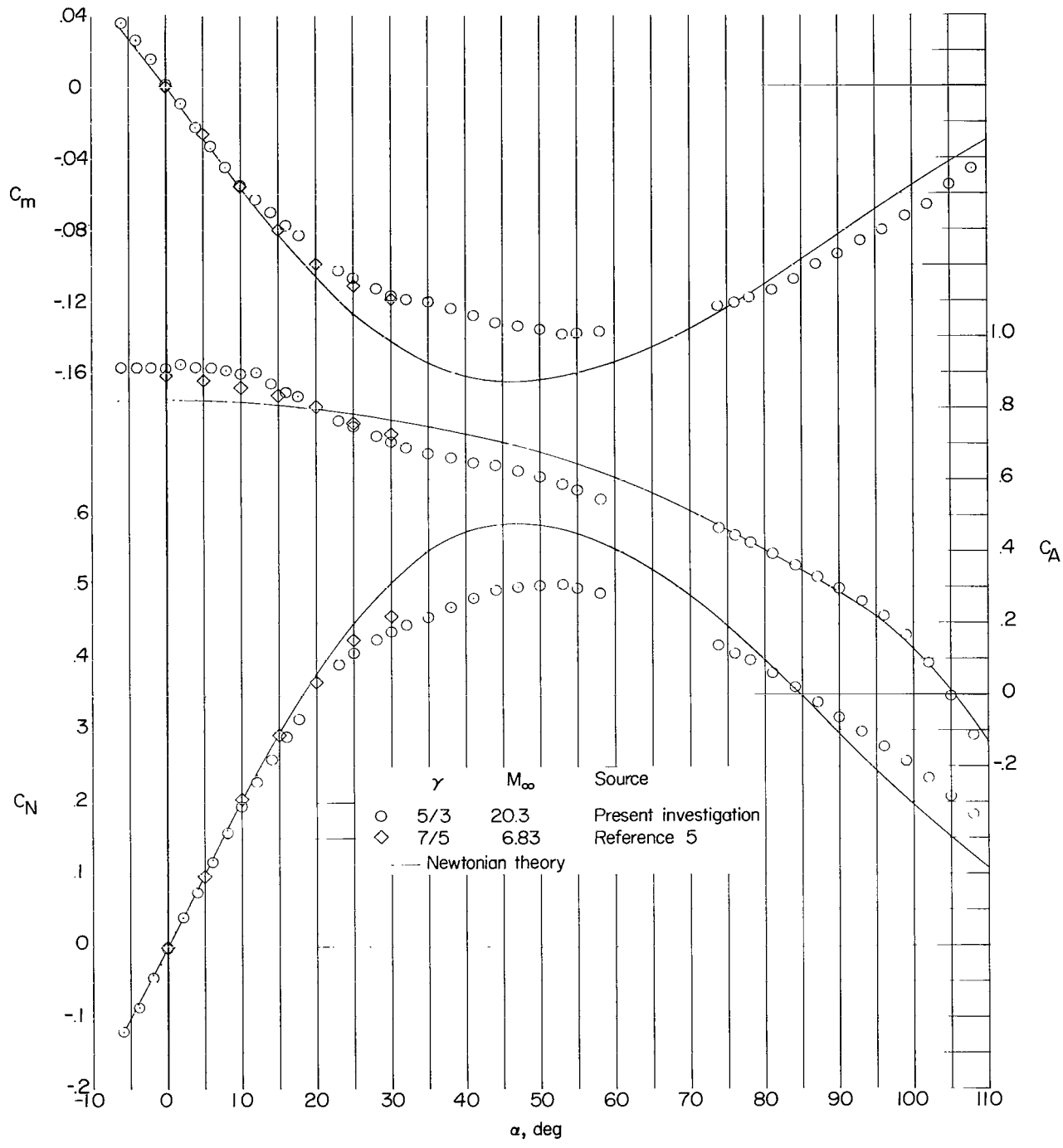


(f) $\theta_c = 40^0$.

Figure 5.- Continued.

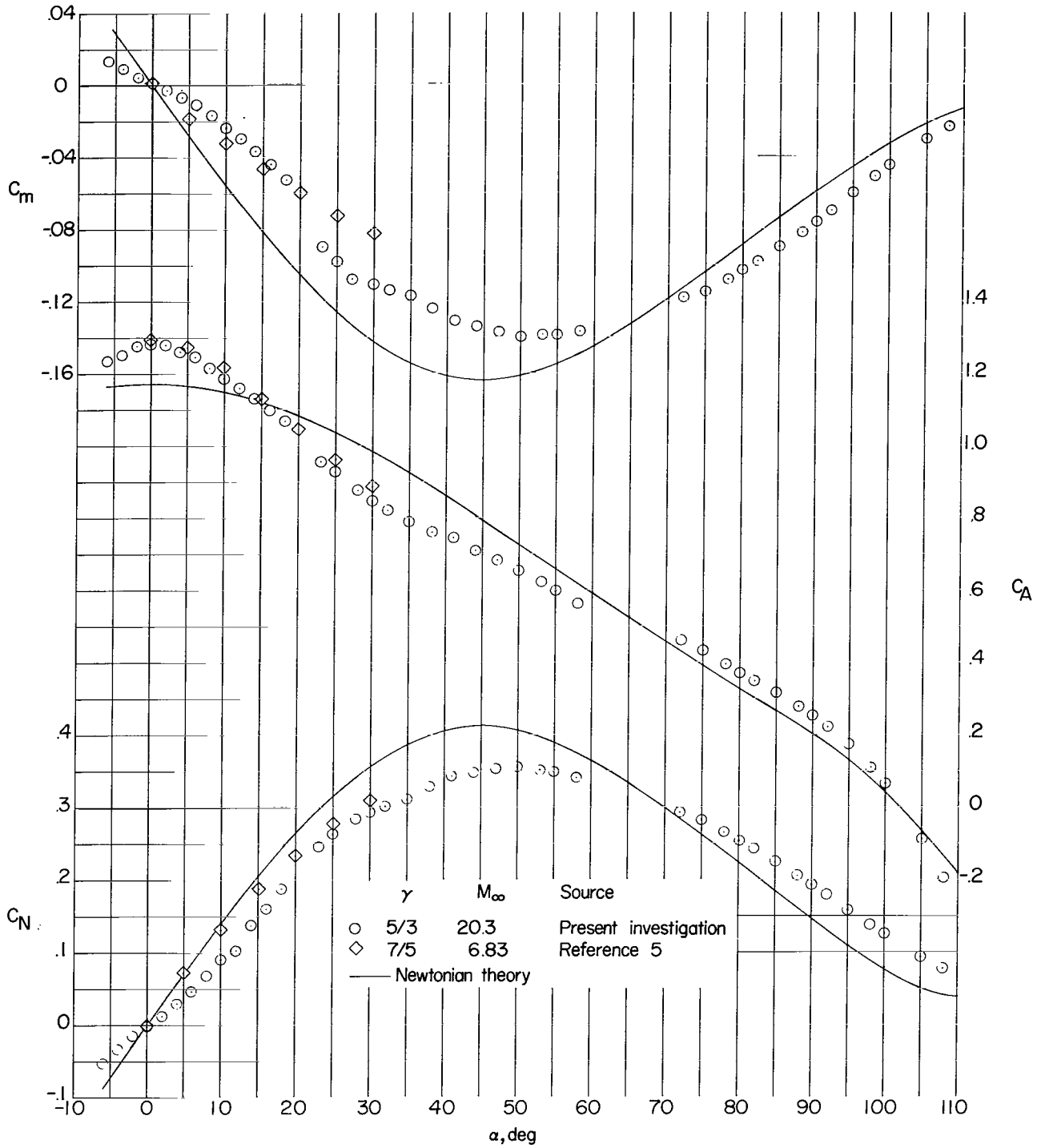


(g) $\theta_c = 50^0$.

Figure 5.- Continued.

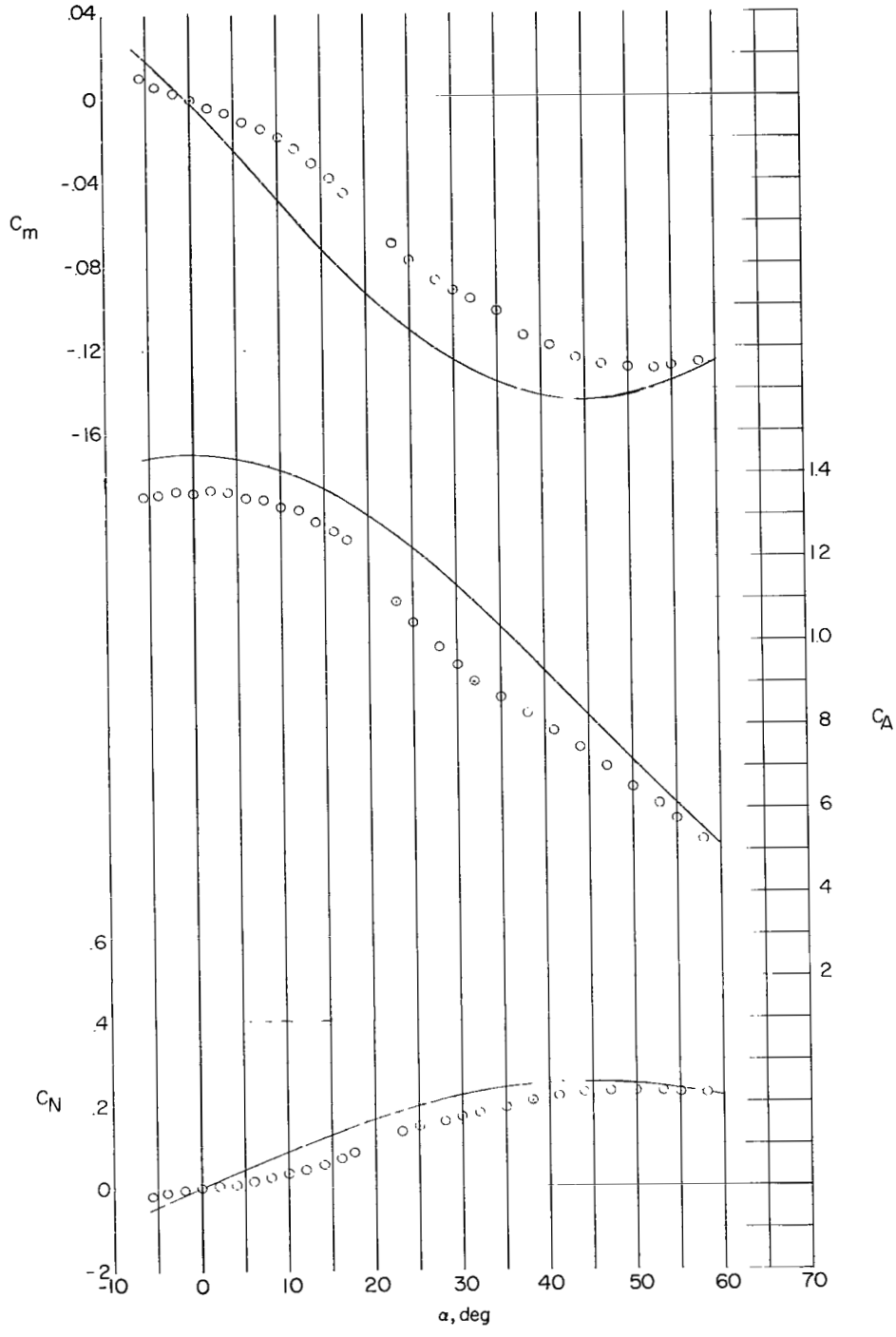


(h) $\theta_c = 60^0$.

Figure 5.- Continued.

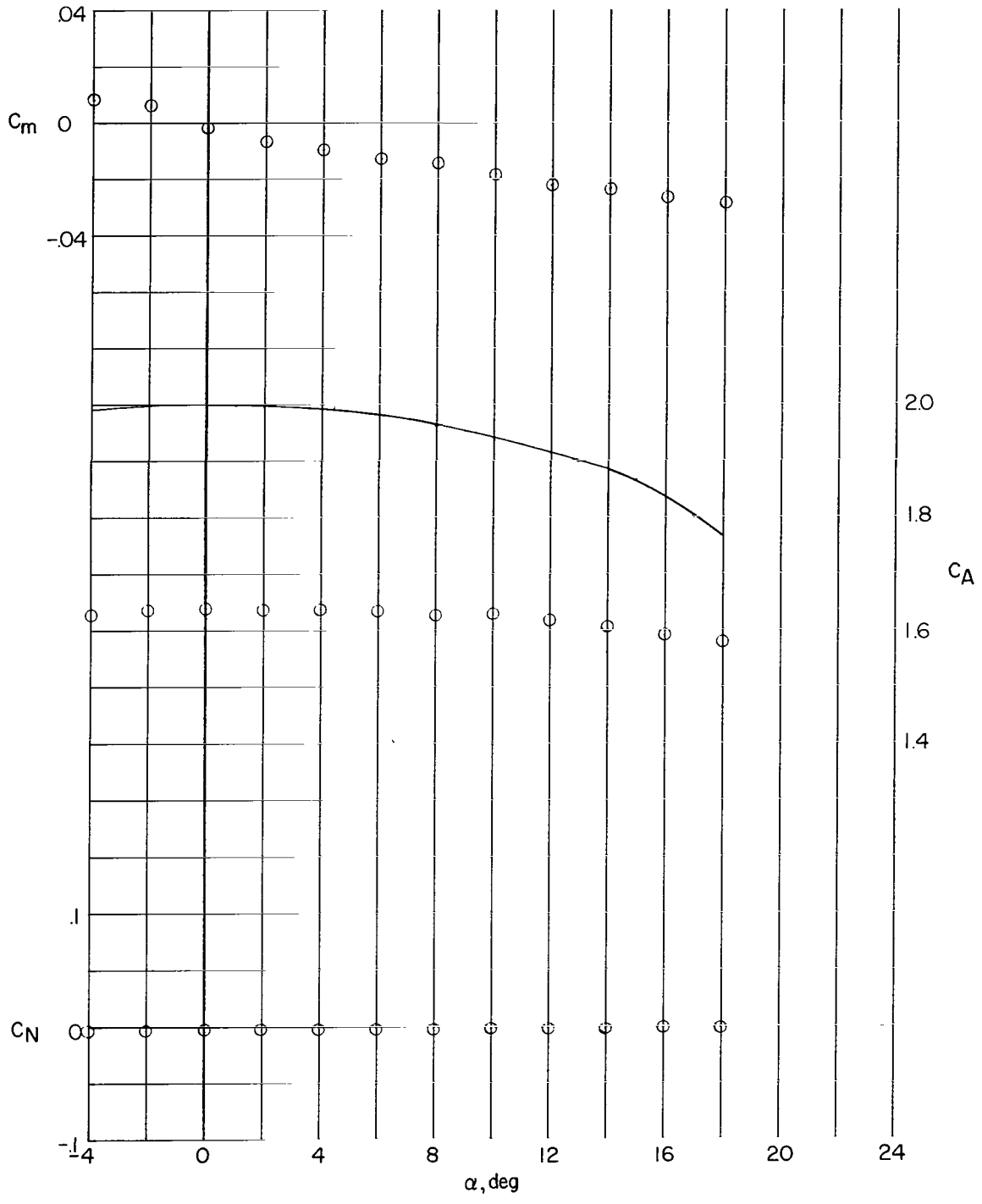


(i) $\theta_c = 90^0$.

Figure 5.- Concluded

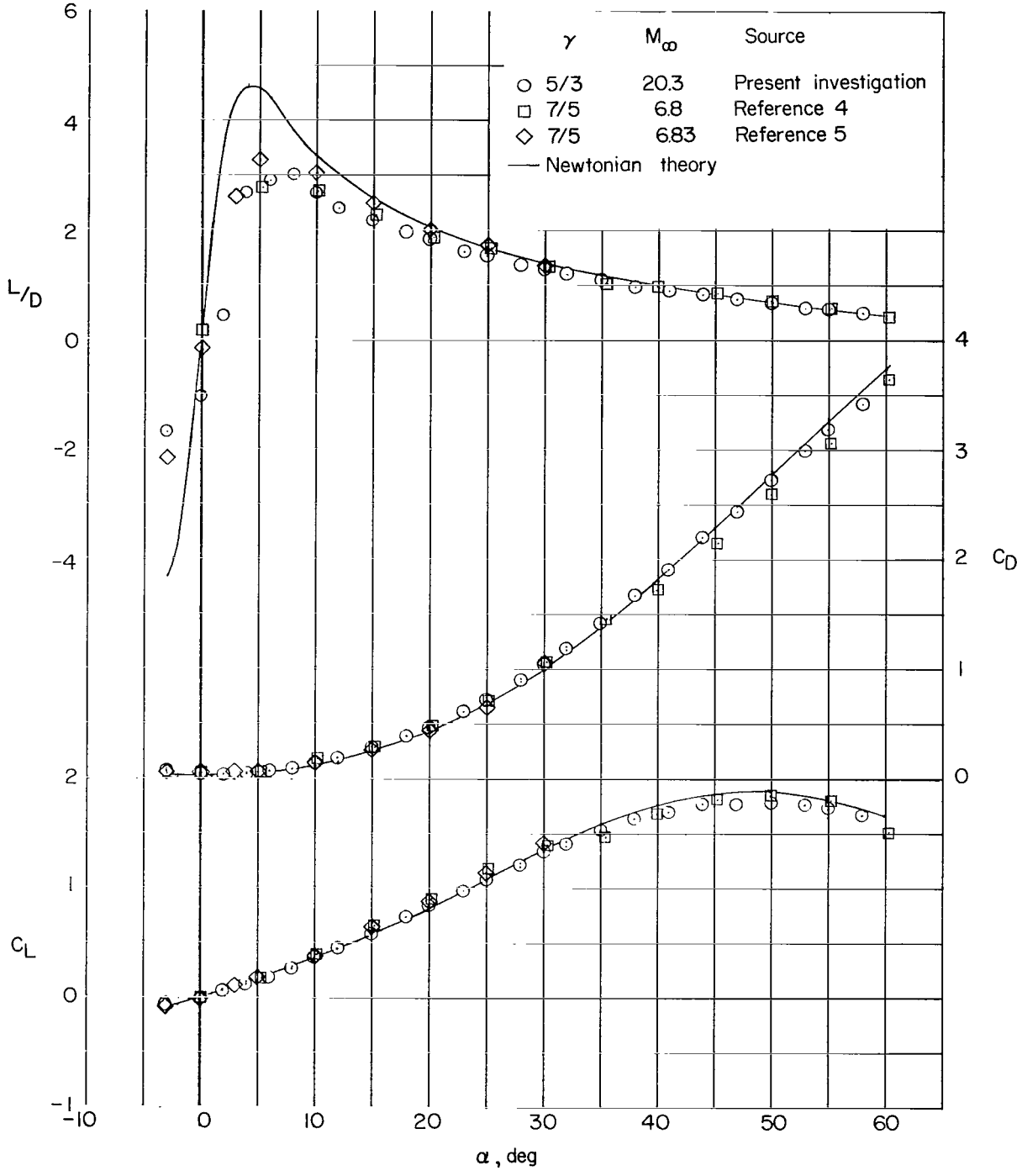


(a) $\theta_c = 5^0$.

Figure 6.- Longitudinal characteristics of sharp right circular cones referred to wind-axis system in air and helium.

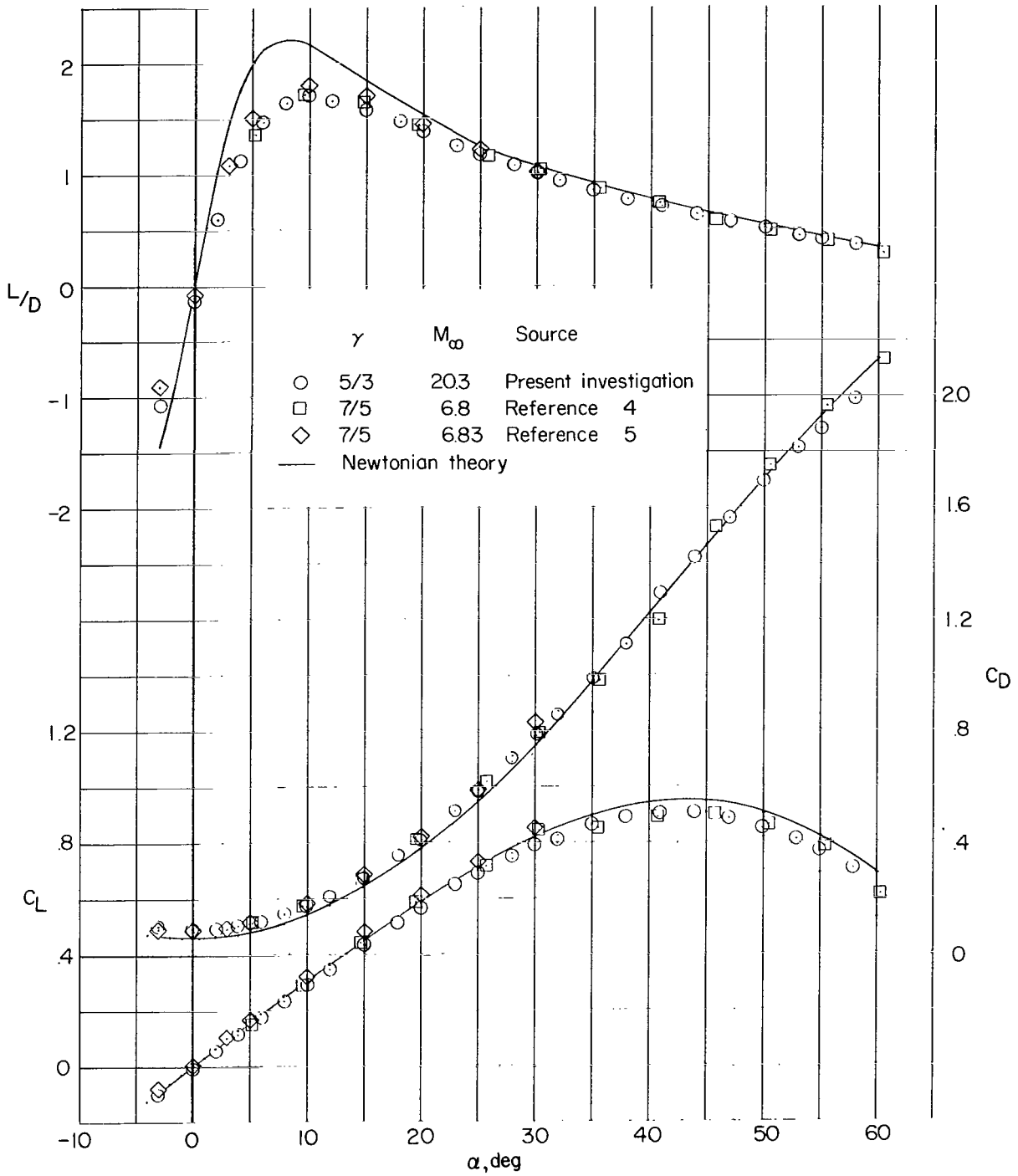


(b) $\theta_c = 10^0$.

Figure 6.- Continued.

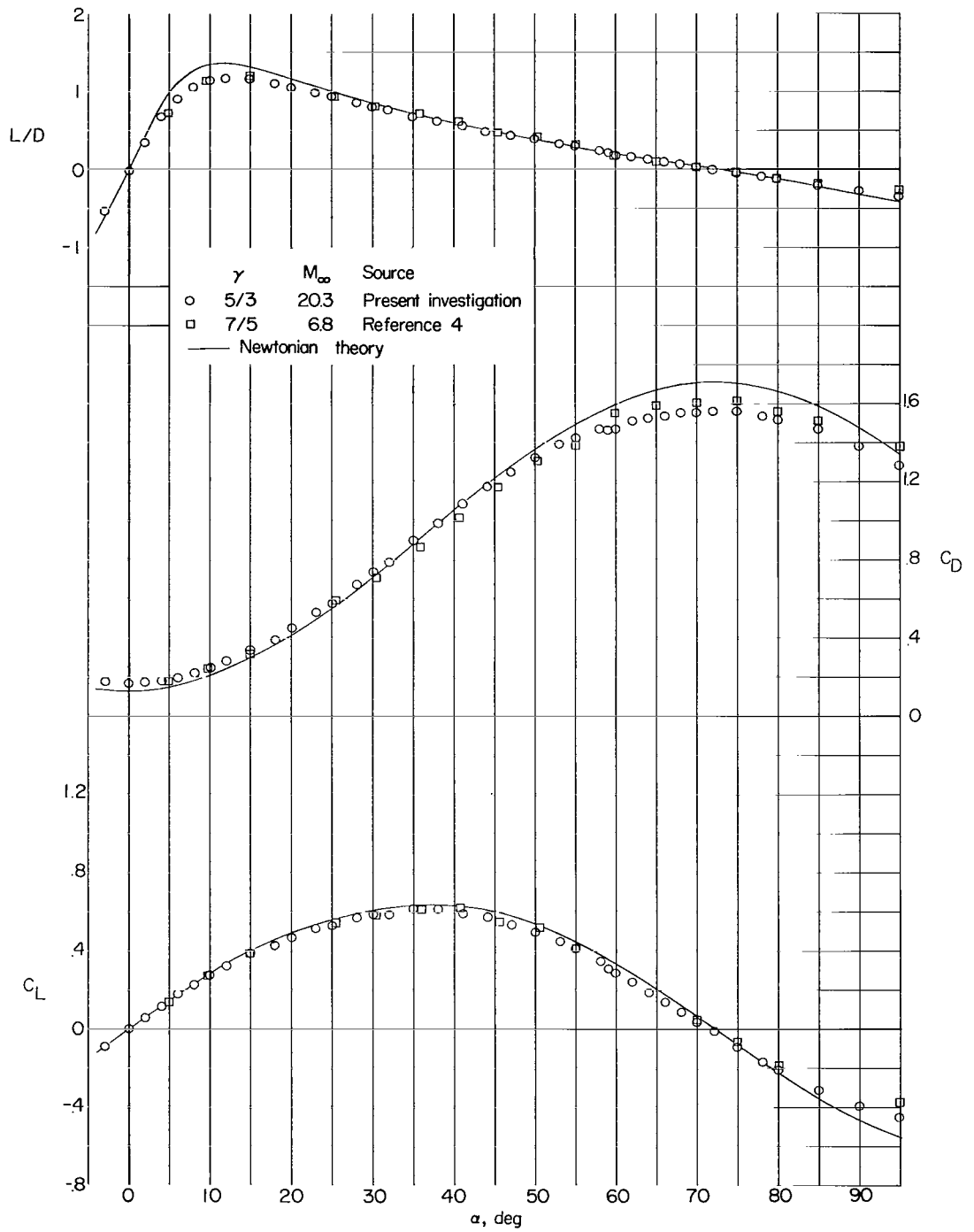


(c) $\theta_c = 15^0$.

Figure 6.- Continued.

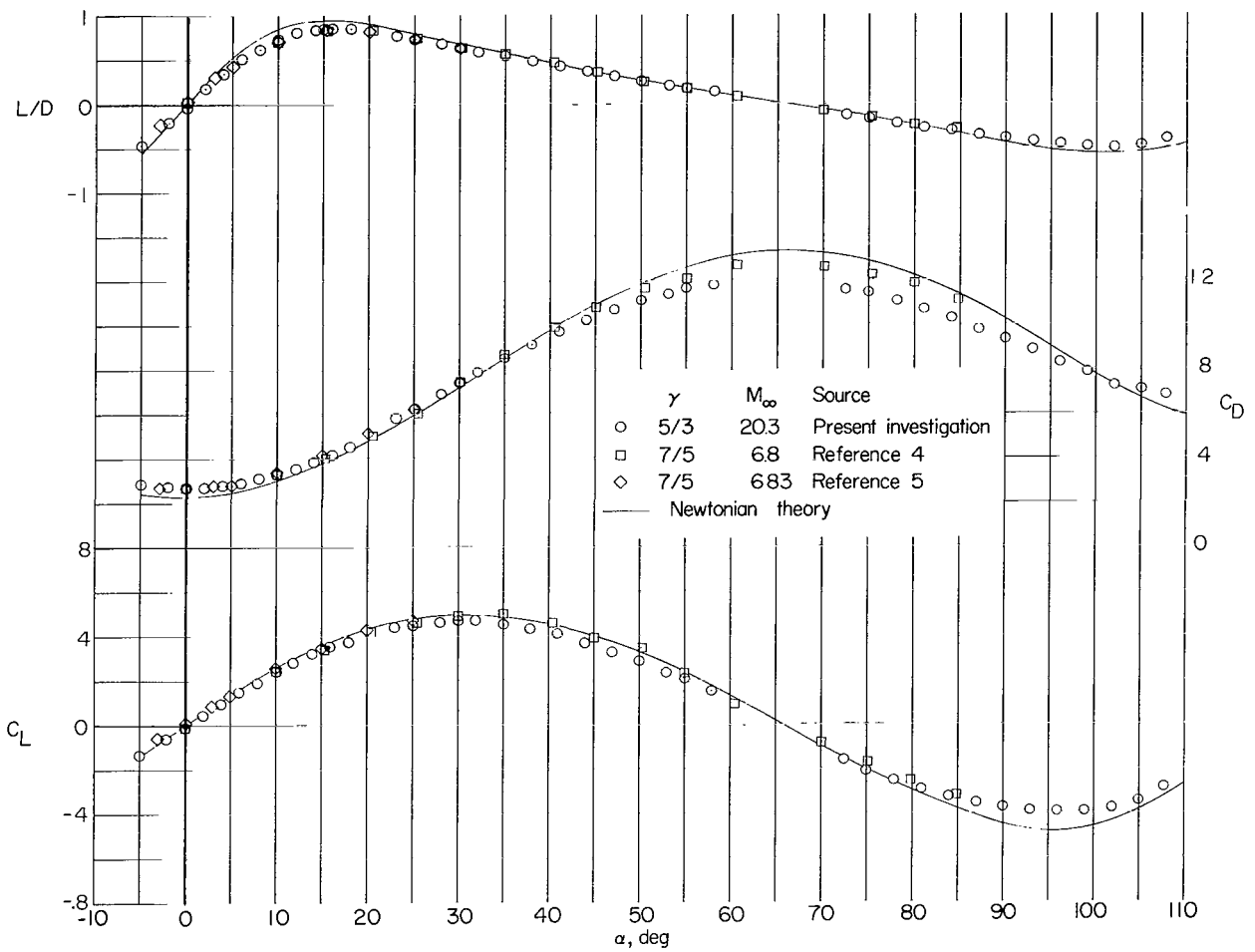


(d) $\theta_c = 20^0$.

Figure 6.- Continued.

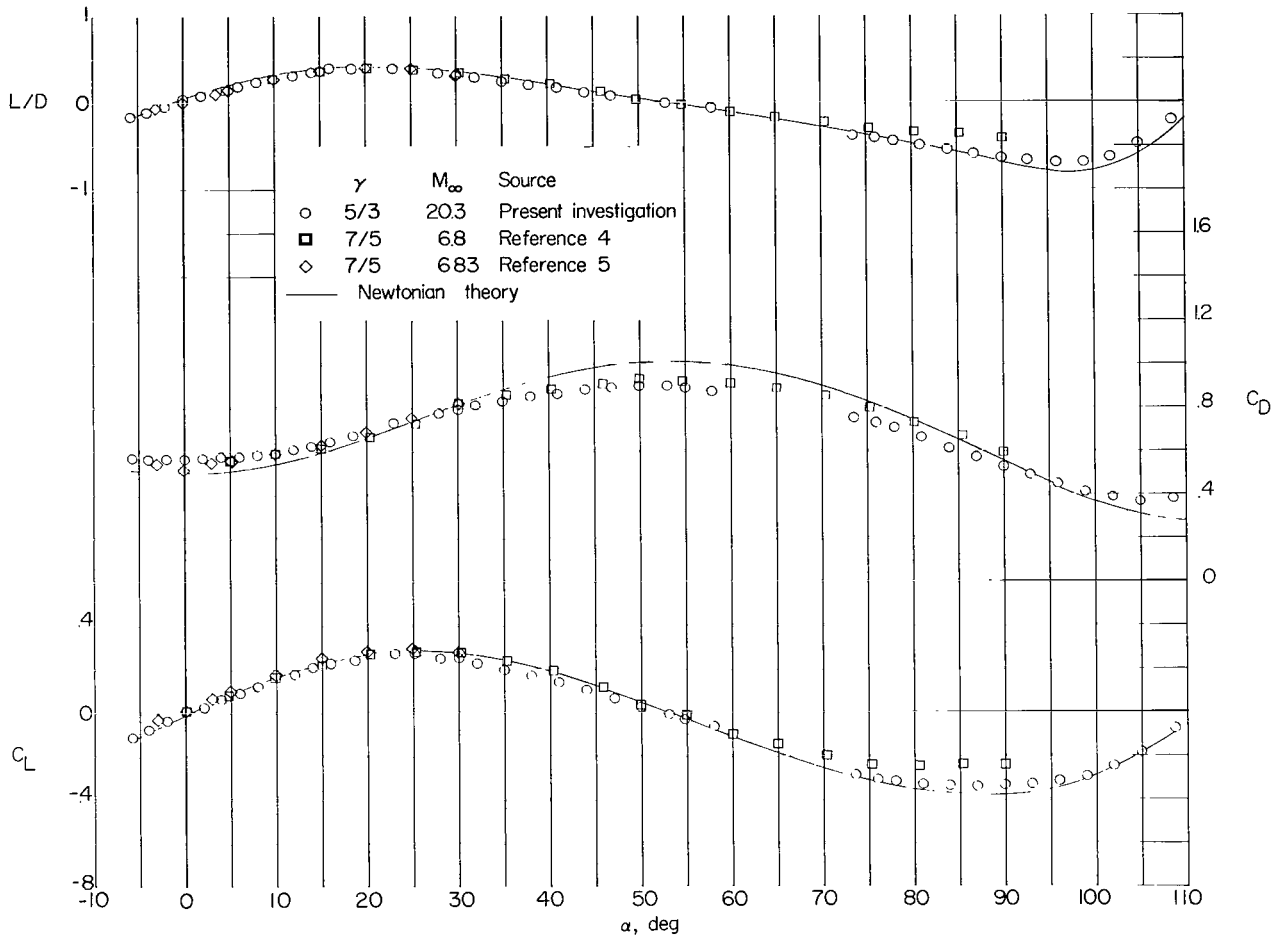


(e) $\theta_c = 30^0$.

Figure 6.- Continued.

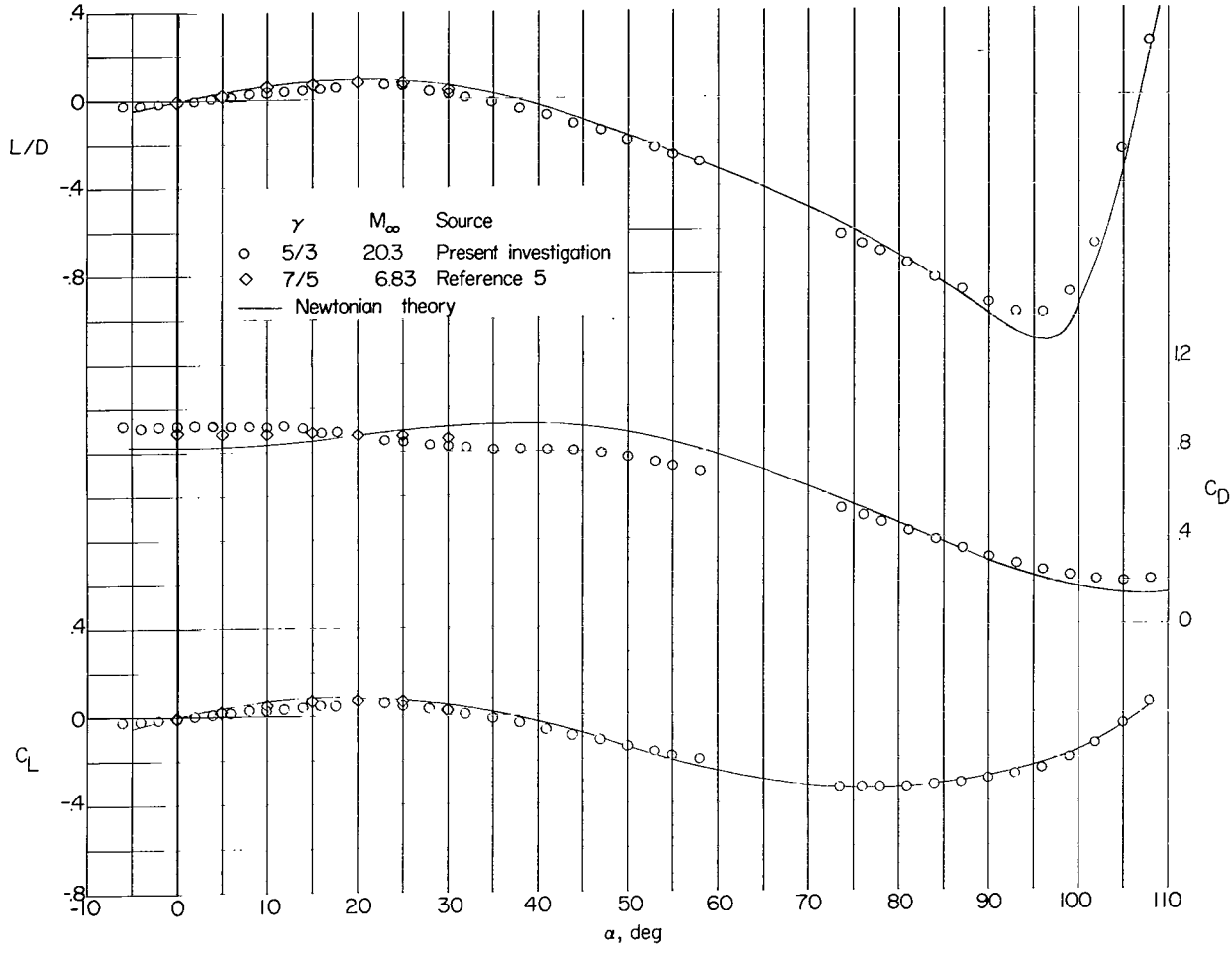


(f) $\theta_c = 40^0$.

Figure 6.- Continued.

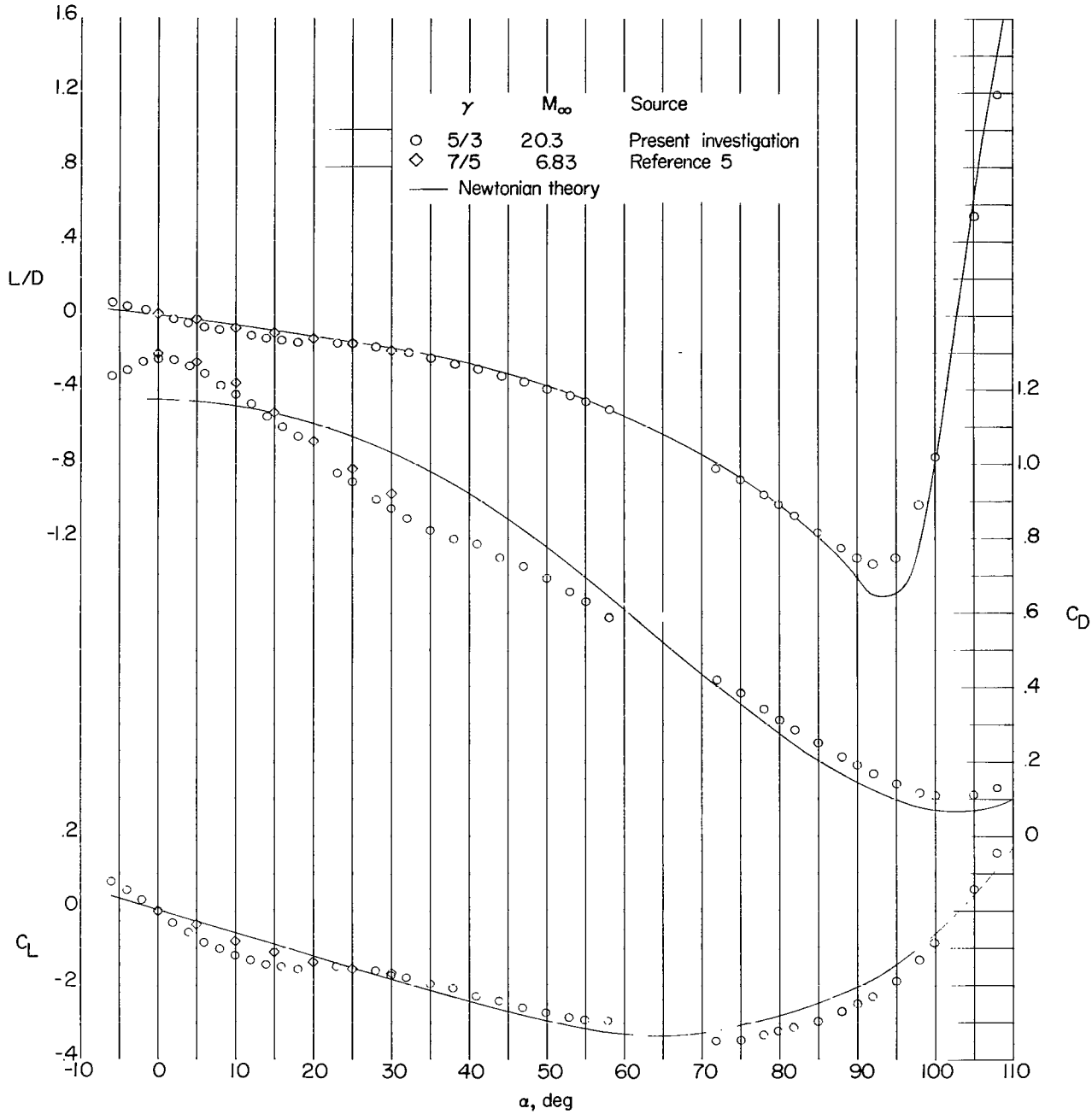


(g) $\theta_c = 50^0$.

Figure 6.- Continued.

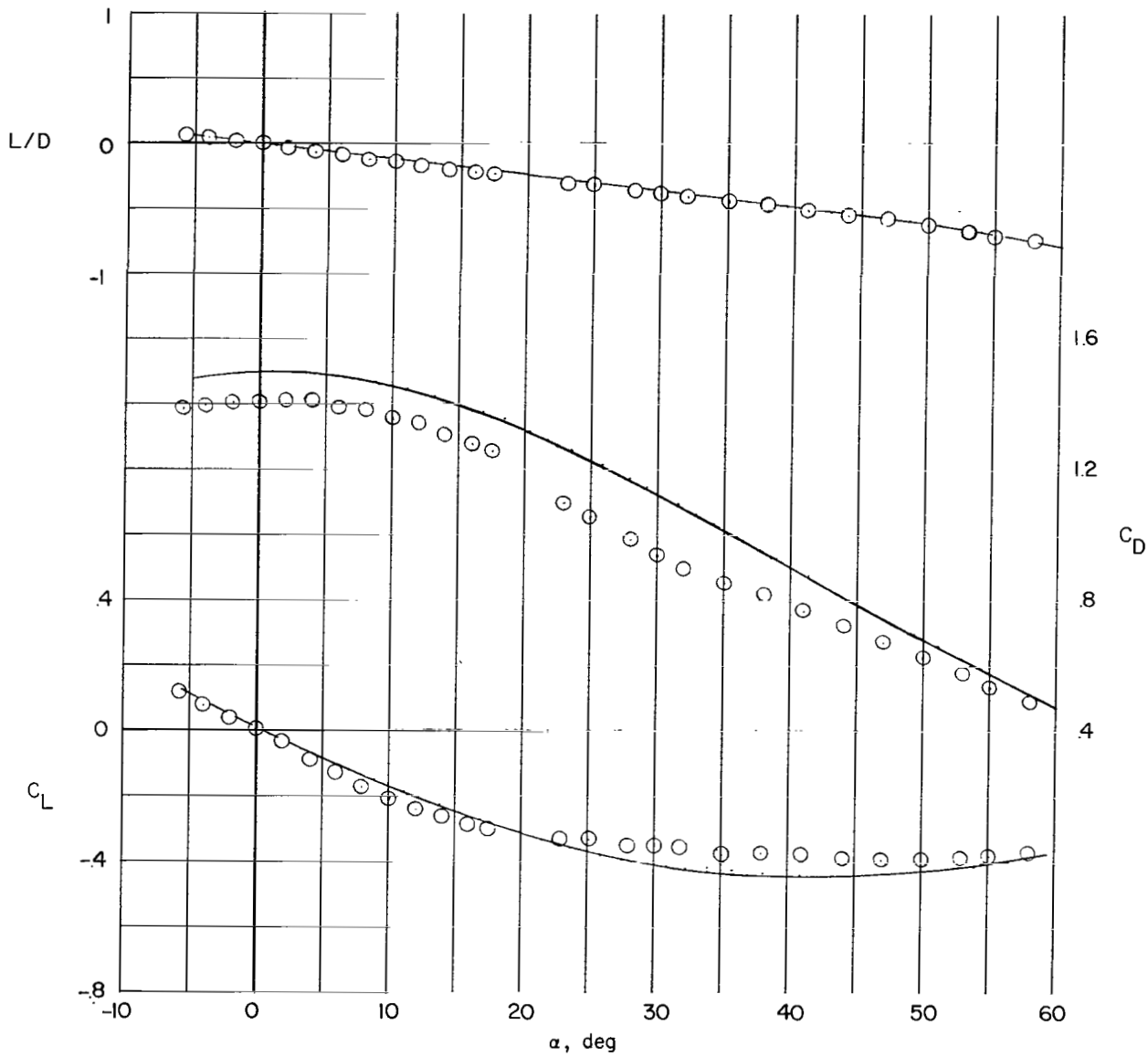


(h) $\theta_c = 60^0$.

Figure 6.- Continued.

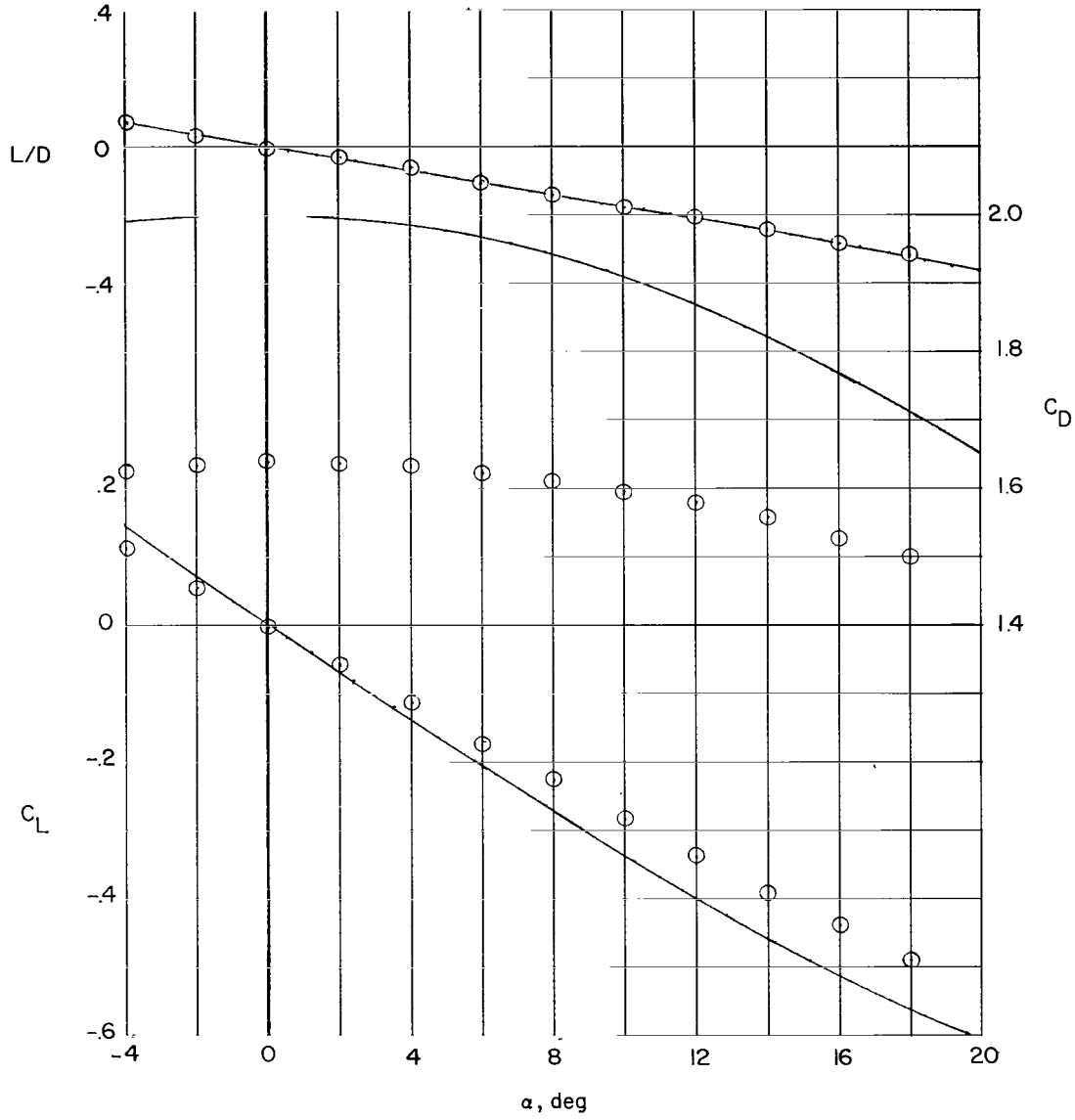


(i) $\theta_c = 90^0$.

Figure 6.- Concluded.

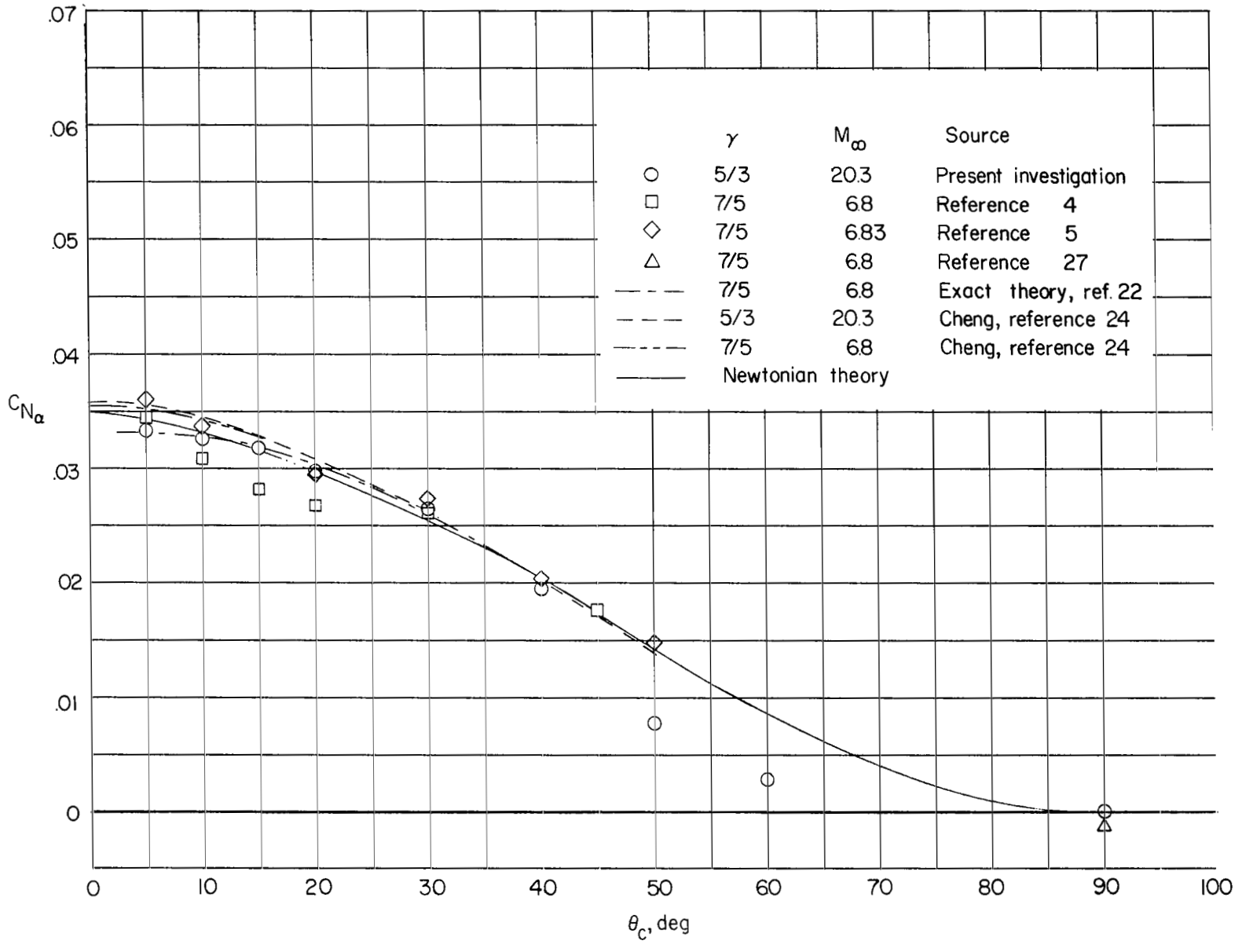


Figure 7.- Variation of normal-force-curve slope with cone angle for sharp right circular cones in air and helium.

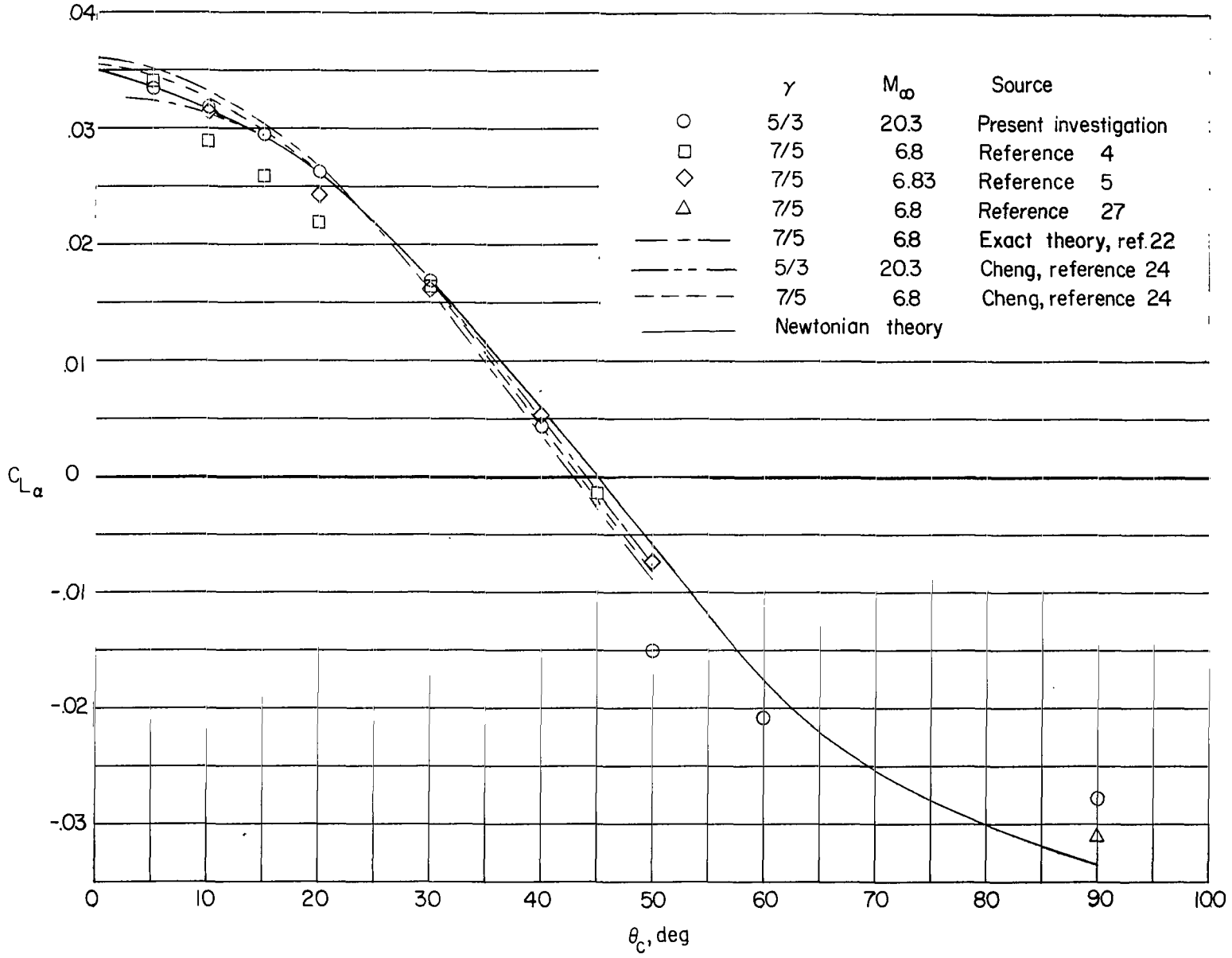


Figure 8.- Variation of lift-curve slope with cone angle for sharp right circular cones in air and helium.

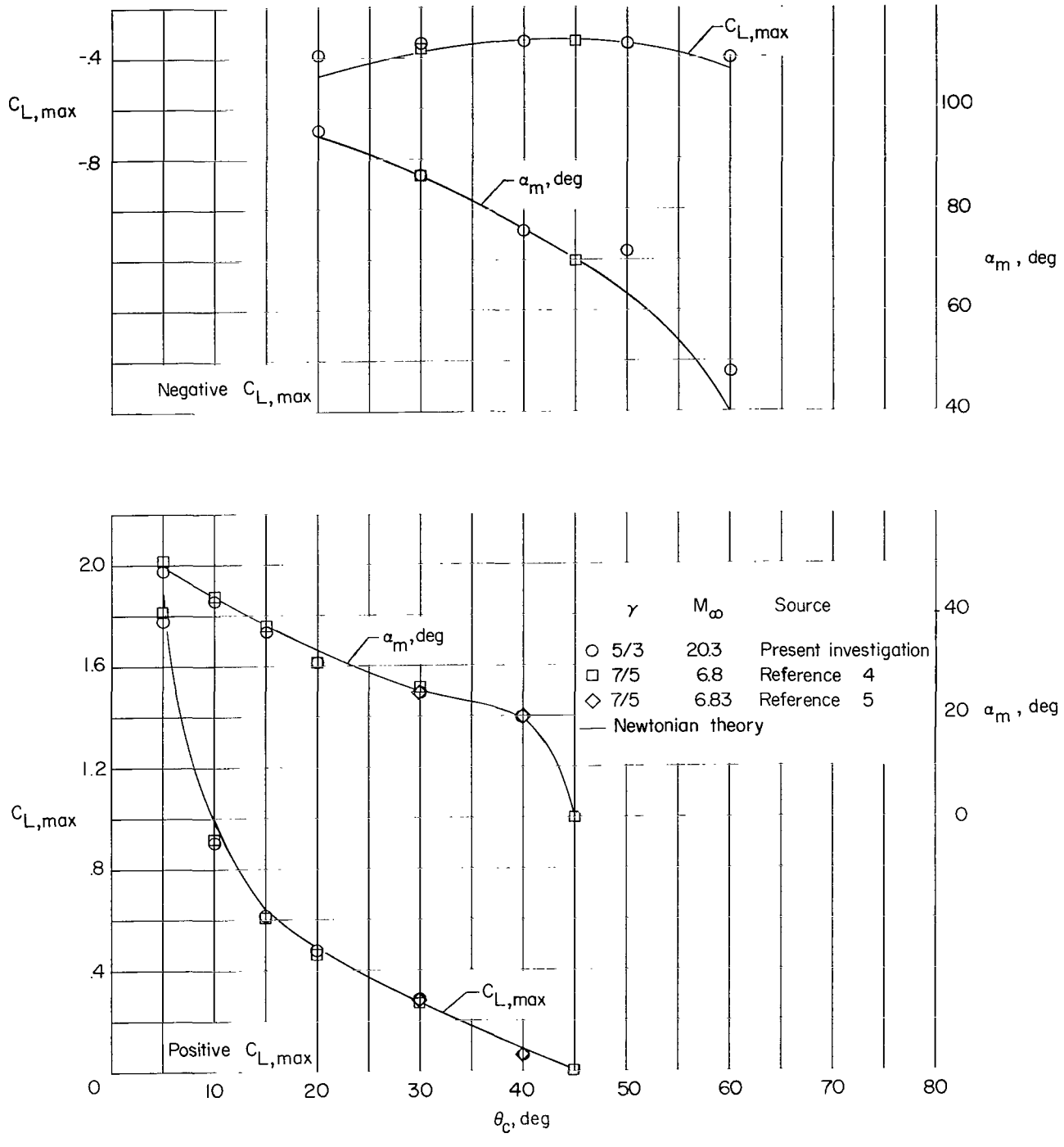


Figure 9.- Variation of maximum positive and negative lift coefficients and angle of attack at which they occur with cone angle for sharp right circular cones in air and helium.

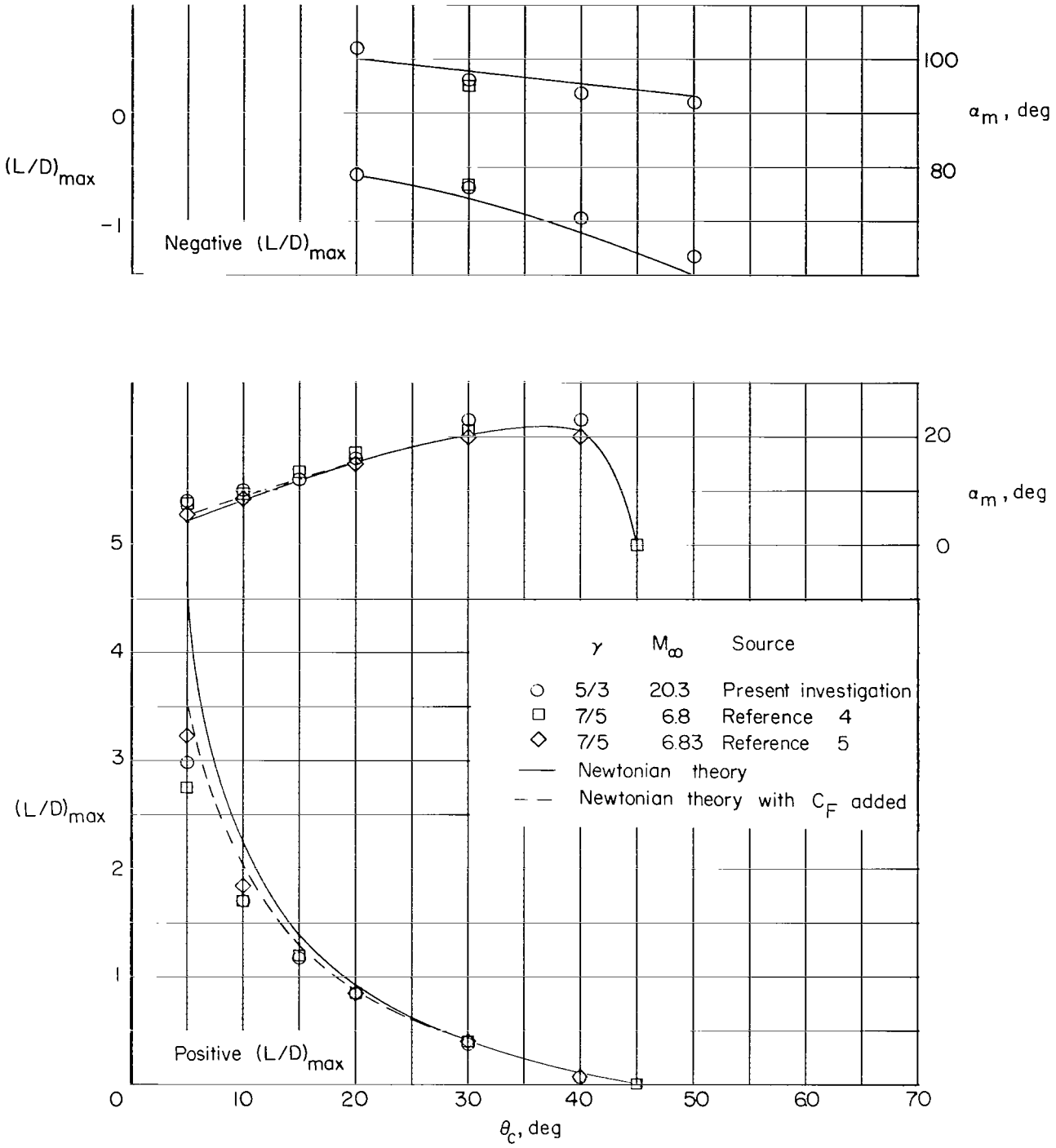


Figure 10.- Variation of maximum positive and negative lift-drag ratios and angle of attack at which they occur with cone angle for sharp right circular cones in air and helium.

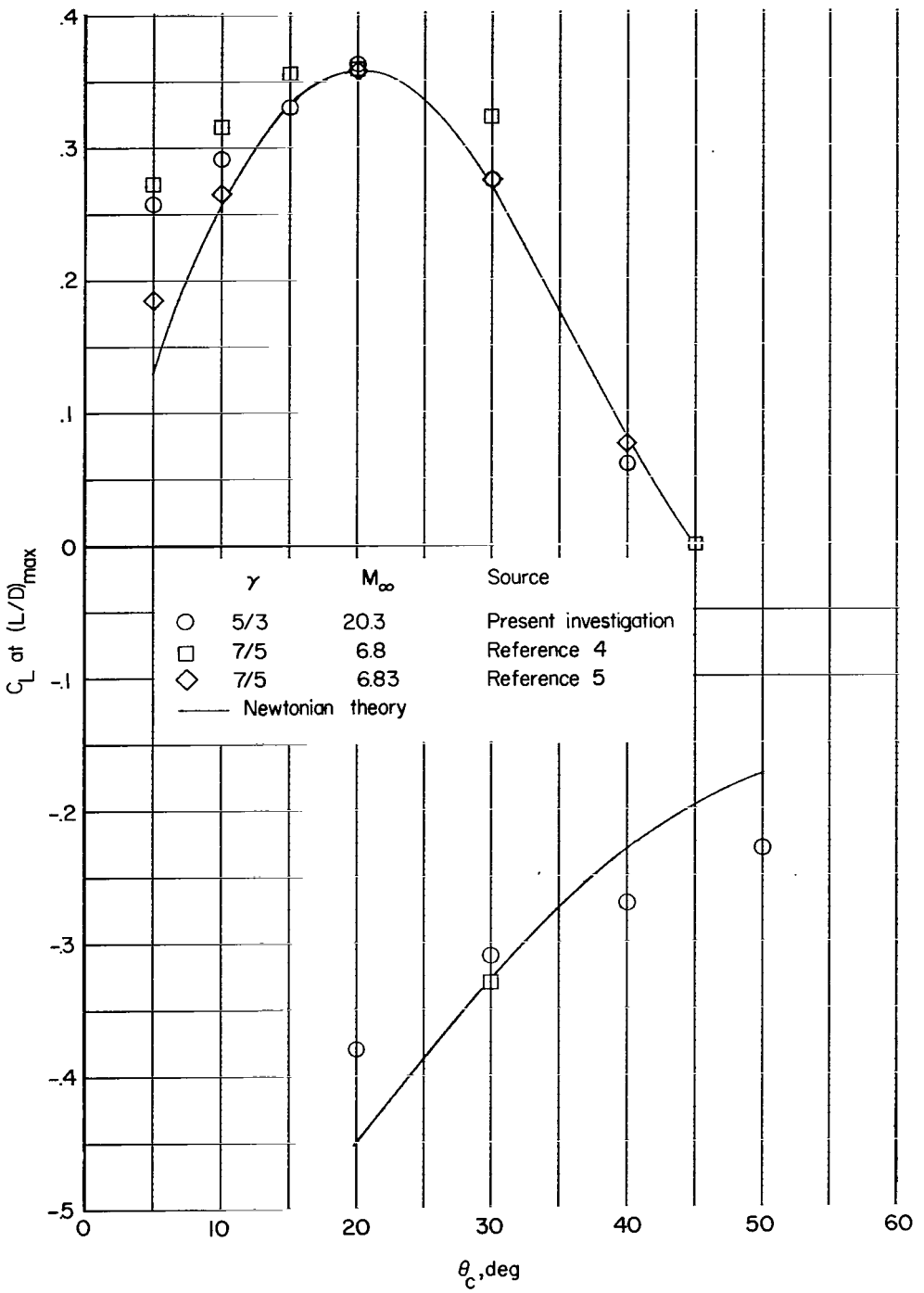


(a) $C_L$ at $(L/D)_{max}$.

Figure 11.- Variation of lift coefficient for maximum positive and negative lift-drag ratios and lift-drag ratio for maximum positive and negative lift coefficients on sharp right circular cones in air and helium.

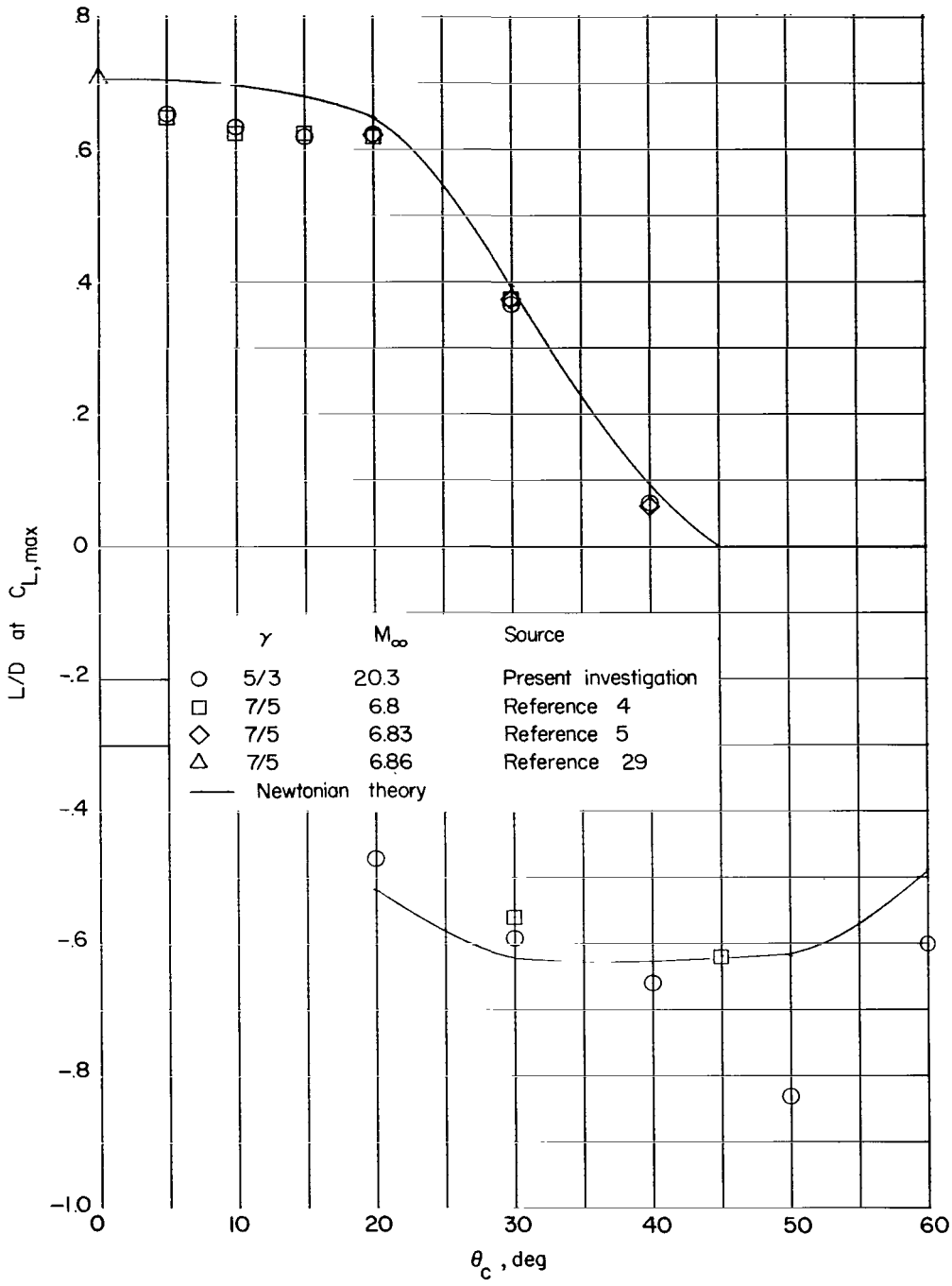


(b) L/D at $C_{L,max}$.

Figure 11.- Concluded.

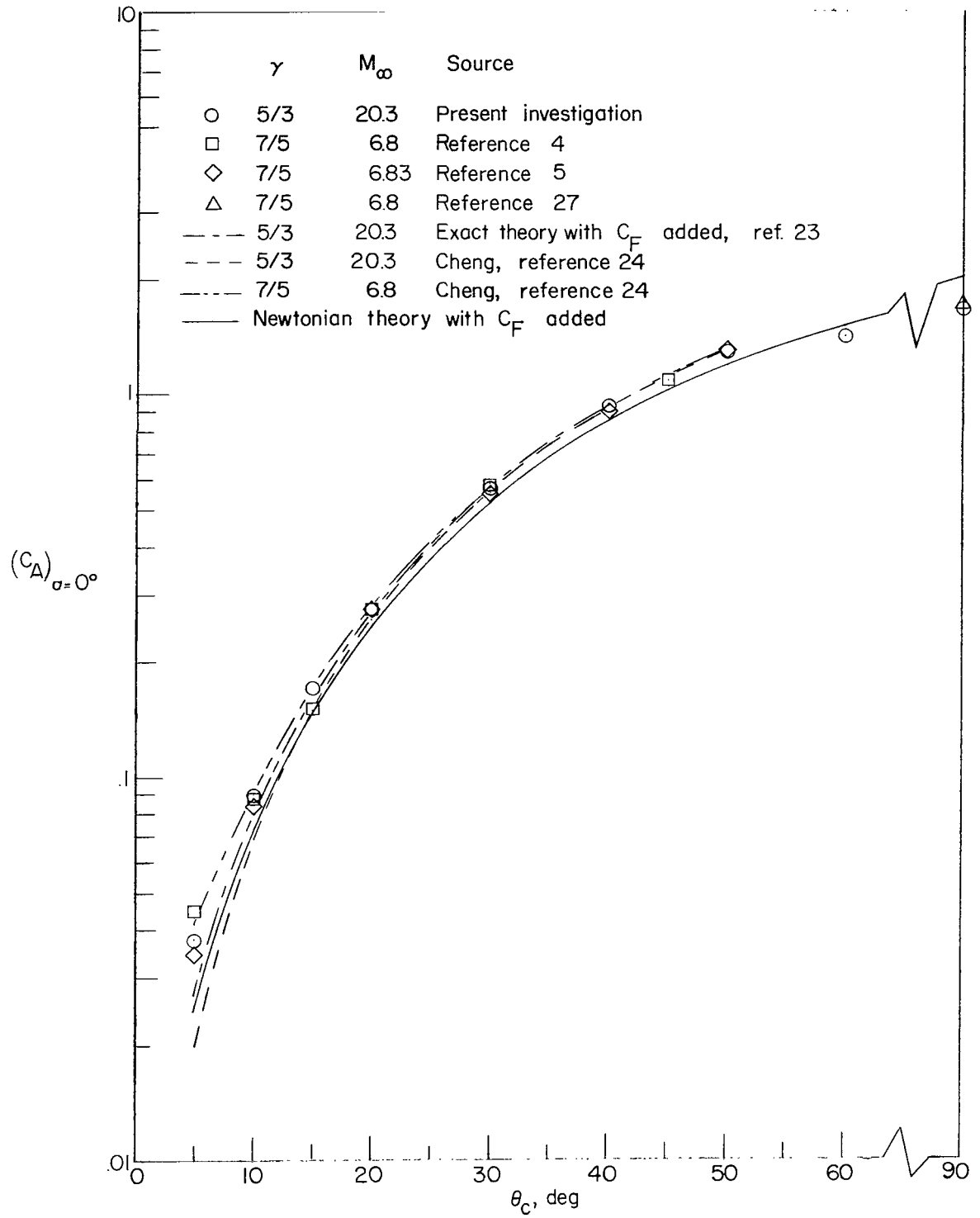


Figure 12.- Variation of axial-force coefficient at $\alpha = 0^0$ with cone angle for right circular cones in air and helium.

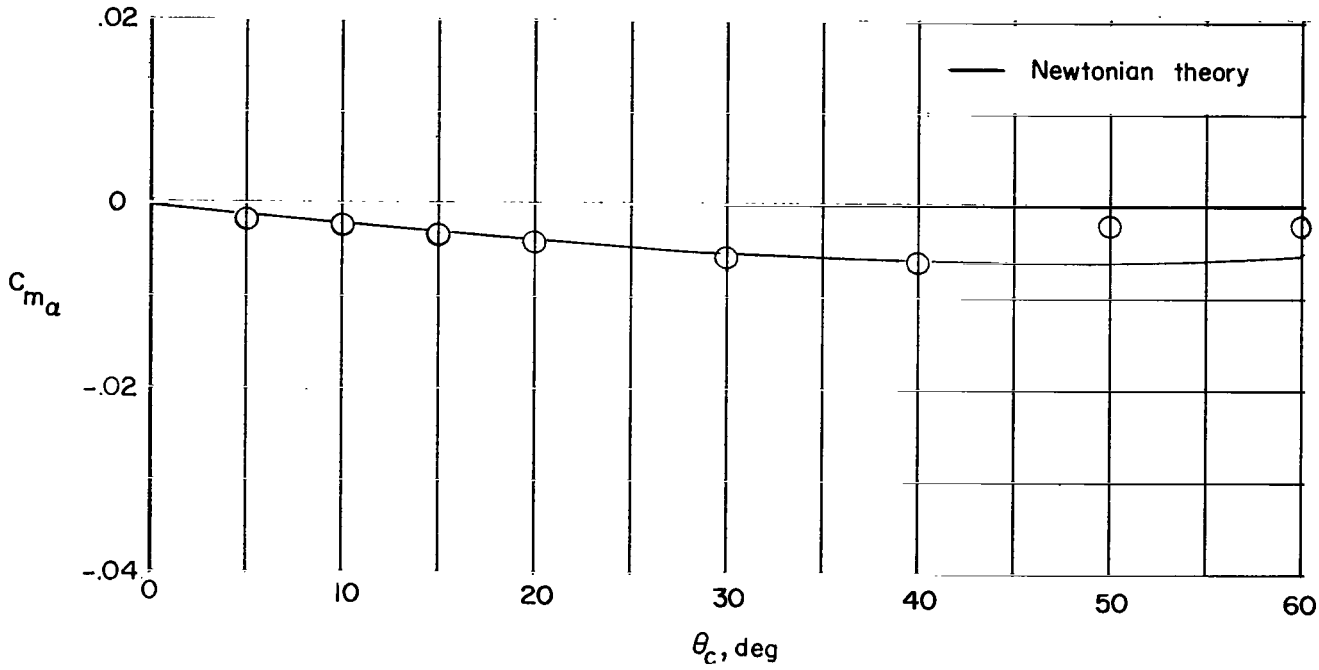


Figure 13.- Variation of pitching-moment-curve slope for sharp right circular cones in helium at $M_\infty = 20.3$.

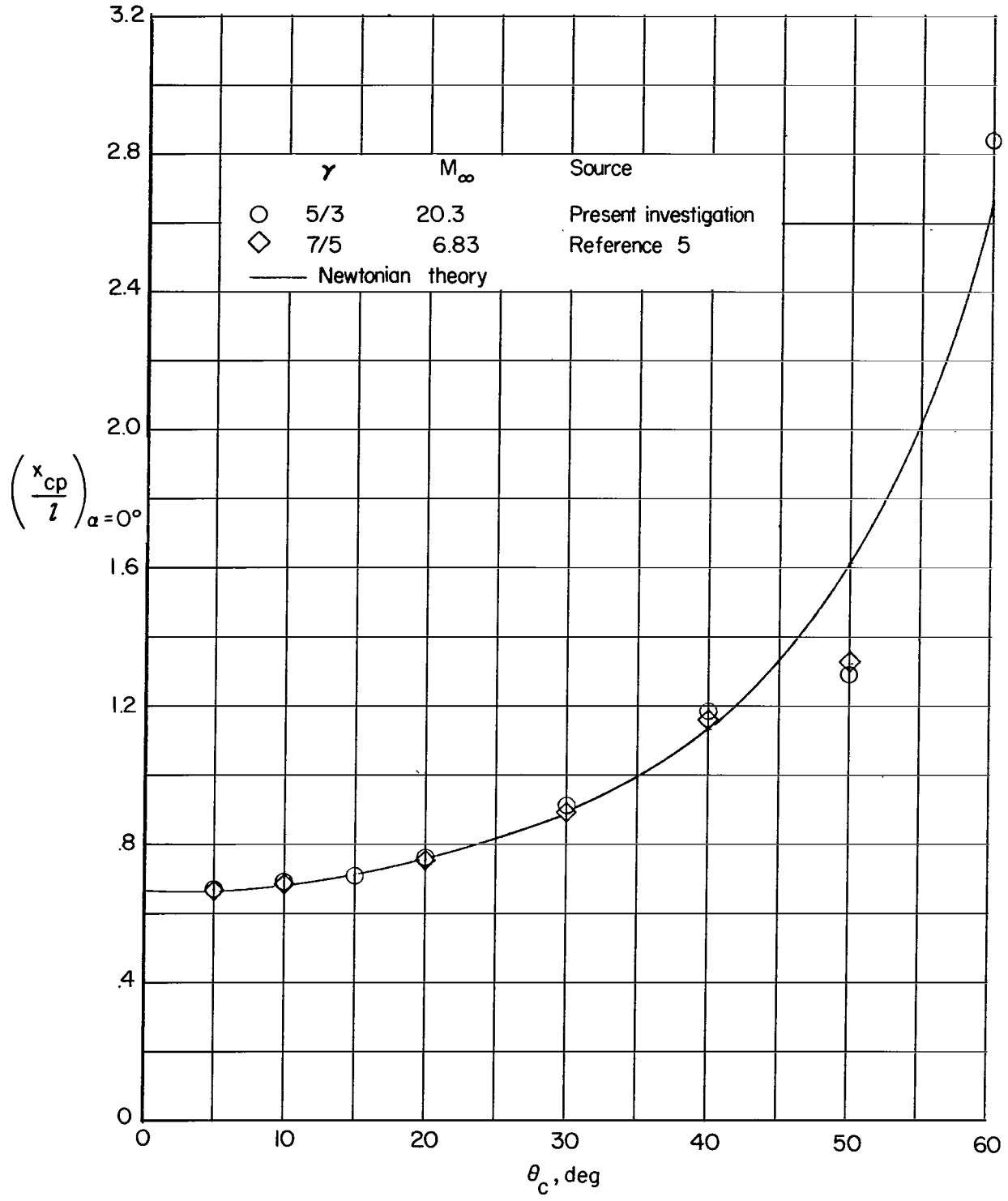


Figure 14.- Variation of initial center-of-pressure location with cone angle for sharp right circular cones in air and helium.

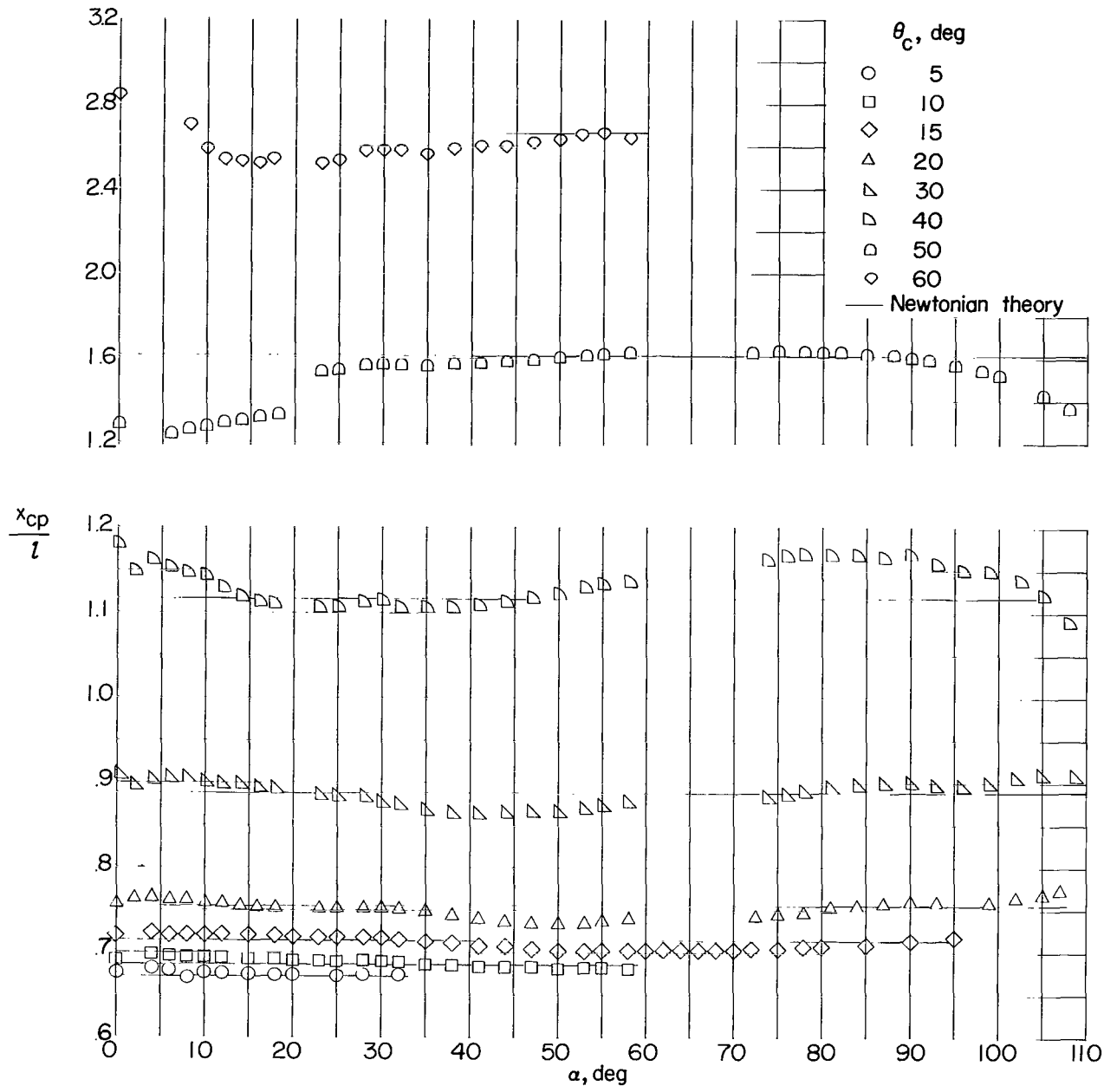


Figure 15.- Variation of center-of-pressure location with angle of attack for sharp right circular cones in helium at $M_\infty = 20.3$.

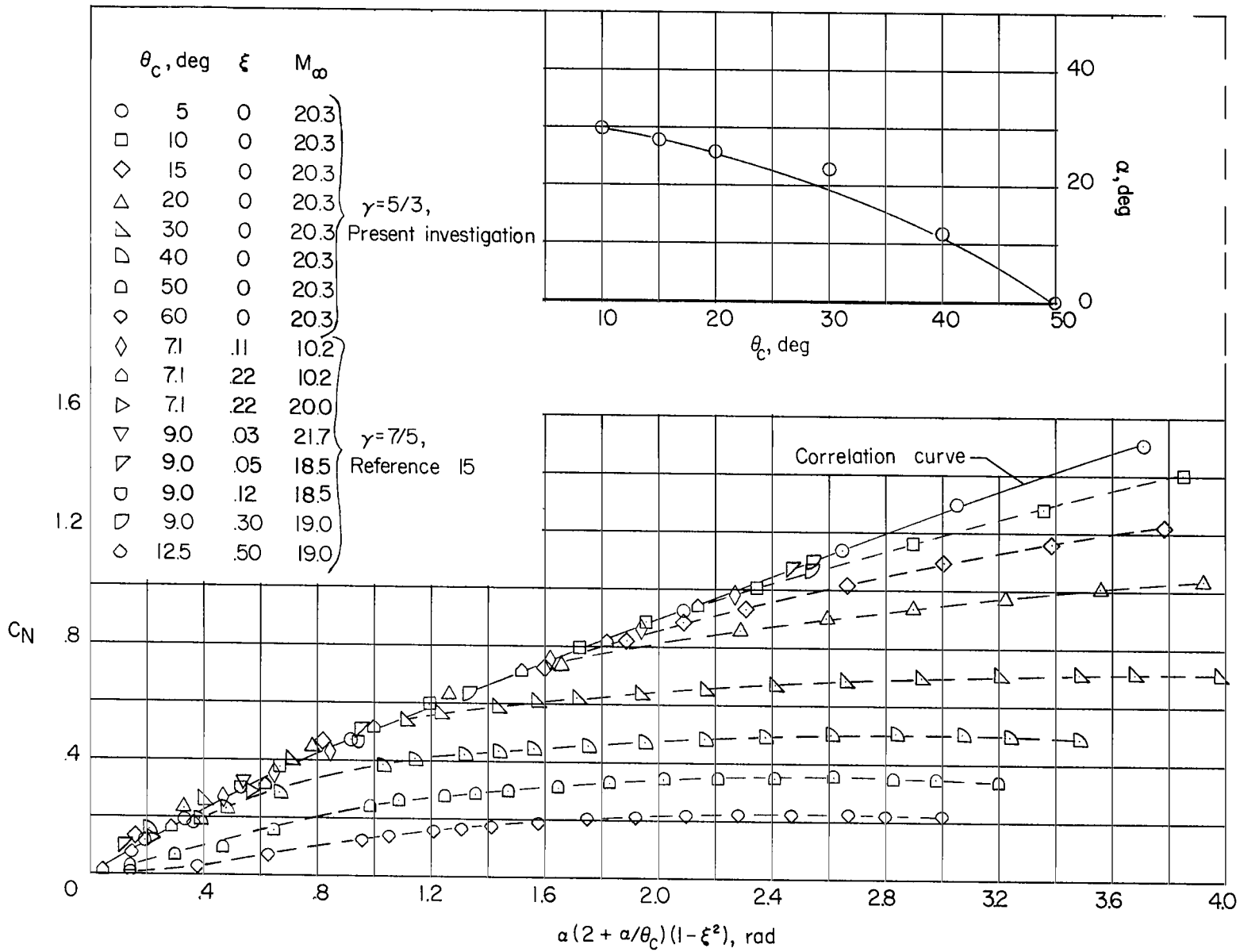


Figure 16.- Correlation of normal-force coefficient on sharp and blunt right circular cones in air and helium.

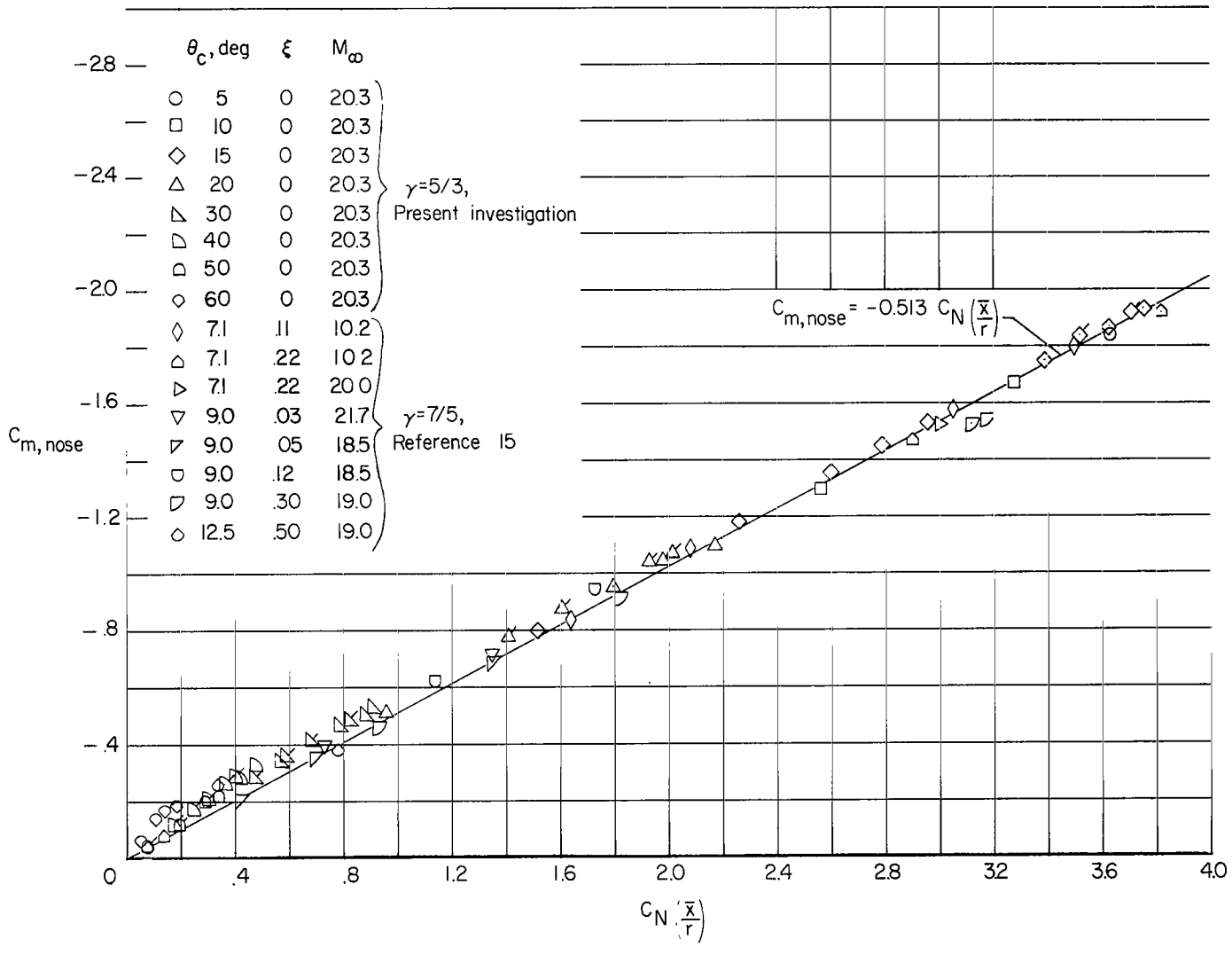


(a) $0 \leq C_N\left(\frac{\bar{x}}{r}\right) \leq 4.0$.

Figure 17.- Correlation of pitching-moment coefficient on sharp and blunt right circular cones in air and helium. Flag indicates values of $C_m$ beyond those for $C_{N,max}$.

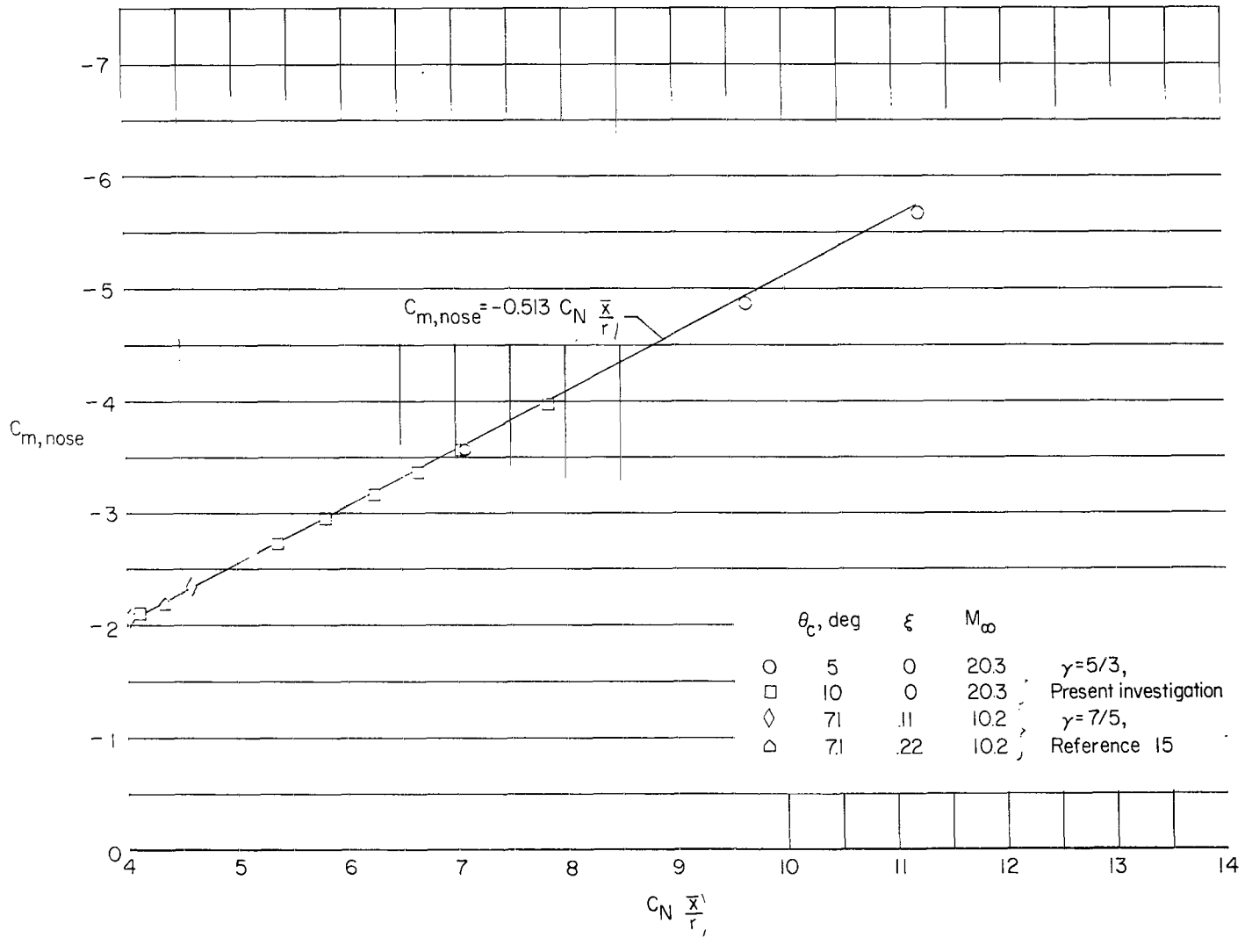


(b) $4.0 \leq C_N\left(\frac{\bar{x}}{r}\right) \leq 14$.

Figure 17.- Concluded.

*"The aeronautical and space activities of the United States shall be conducted so as to contribute . . . to the expansion of human knowledge of phenomena in the atmosphere and space. The Administration shall provide for the widest practicable and appropriate dissemination of information concerning its activities and the results thereof."*

—NATIONAL AERONAUTICS AND SPACE ACT OF 1958

# NASA SCIENTIFIC AND TECHNICAL PUBLICATIONS

TECHNICAL REPORTS: Scientific and technical information considered important, complete, and a lasting contribution to existing knowledge.

TECHNICAL NOTES: Information less broad in scope but nevertheless of importance as a contribution to existing knowledge.

TECHNICAL MEMORANDUMS: Information receiving limited distribution because of preliminary data, security classification, or other reasons.

CONTRACTOR REPORTS: Technical information generated in connection with a NASA contract or grant and released under NASA auspices.

TECHNICAL TRANSLATIONS: Information published in a foreign language considered to merit NASA distribution in English.

TECHNICAL REPRINTS: Information derived from NASA activities and initially published in the form of journal articles.

SPECIAL PUBLICATIONS: Information derived from or of value to NASA activities but not necessarily reporting the results of individual NASA-programmed scientific efforts. Publications include conference proceedings, monographs, data compilations, handbooks, sourcebooks, and special bibliographies.

***Details on the availability of these publications may be obtained from:***

**SCIENTIFIC AND TECHNICAL INFORMATION DIVISION**

**NATIONAL AERONAUTICS AND SPACE ADMINISTRATION**

**Washington, D.C. 20546**